

000 001 TRAINING-FREE DEFENSE AGAINST ADVERSARIAL 002 ATTACKS IN DEEP LEARNING MRI RECONSTRUCTION 003 004

005 **Anonymous authors**

006 Paper under double-blind review

007 008 ABSTRACT 009

011 Deep learning (DL) methods have become the state-of-the-art for reconstructing
012 sub-sampled magnetic resonance imaging (MRI) data. However, studies have
013 shown that these methods are susceptible to small adversarial input perturbations,
014 or attacks, resulting in major distortions in the output images. Various strategies
015 have been proposed to reduce the effects of these attacks, but they require re-
016 training and may lower reconstruction quality for non-perturbed/clean inputs. In
017 this work, we propose a novel approach for mitigating adversarial attacks on MRI
018 reconstruction models without any retraining. Based on the idea of cyclic mea-
019 surement consistency, we devise a novel mitigation objective that is minimized in
020 a small ball around the attack input. Results show that our method substantially
021 reduces the impact of adversarial perturbations across different datasets, attack
022 types/strengths and PD-DL networks, and qualitatively and quantitatively outper-
023 forms conventional mitigation methods that involve retraining. We also introduce
024 a practically relevant scenario for small adversarial perturbations that models im-
025 pulse noise in raw data, which relates to *herringbone artifacts*, and show the appli-
026 cability of our approach in this setting. Finally, we show our mitigation approach
027 remains effective in two *realistic* extension scenarios: a blind setup, where the
028 attack strength or algorithm is not known to the user; and an adaptive attack setup,
029 where the attacker has full knowledge of the defense strategy.

030 1 INTRODUCTION

031 Magnetic resonance imaging (MRI) is an essential imaging modality in medical sciences, providing
032 high-resolution images without ionizing radiation, and offering diverse soft-tissue contrast. How-
033 ever, its inherently long acquisition times may lead to patient discomfort and increased likelihood
034 of motion artifacts, which degrade image quality. Accelerated MRI techniques obtain a reduced
035 number of measurements below Nyquist rate and reconstruct the image by incorporating supple-
036 mentary information. Parallel imaging, which is the most clinically used approach, leverages the
037 inherent redundancies in the data from receiver coils (Pruessmann et al., 1999), while compressed
038 sensing (CS) utilizes the compressibility of images through linear sparsifying transforms to achieve
039 a regularized reconstruction (Lustig et al., 2007; Jung et al., 2009). Recently, deep learning (DL)
040 methods have emerged as the state-of-the-art for accelerated MRI, offering superior reconstruction
041 quality compared to traditional techniques (Hammerink et al., 2018; Knoll et al., 2020a; Akçakaya
042 et al., 2022). In particular, physics-driven DL (PD-DL) reconstruction has become popular due to
043 their improved generalizability and performance (Hammerink et al., 2018; Aggarwal et al., 2019).

044 While PD-DL methods significantly outperform traditional MRI reconstruction techniques, these
045 approaches have been shown to be vulnerable to small adversarial perturbations (Goodfellow et al.,
046 2015; Moosavi-Dezfooli et al., 2016), invisible to human observers, resulting in significant varia-
047 tions in the network’s outputs (Antun et al., 2020). Various strategies to improve the robustness of
048 PD-DL networks have been proposed to counter adversarial attacks in MRI reconstruction (Cheng
049 et al., 2020; Calivá et al., 2021; Jia et al., 2022; Raj et al., 2020; Liang et al., 2023). However, all
050 these methods require retraining of the network, incurring a high computational cost, while also
051 having a tendency to lead to additional artifacts for clean/non-attack inputs (Tsipras et al., 2019).

052 In this work, we propose a novel mitigation strategy for adversarial attacks on DL-based MRI recon-
053 struction, which does not require *any retraining*. Our approach utilizes the idea of cyclic measure-
054 ment consistency (Zhao & Hu, 2008; Kim et al., 2023; Tachella et al., 2022; Zhang et al., 2024) with

054 synthesized undersampling patterns. The overarching idea for cyclic measurement consistency is to
 055 simulate new measurements from inference results with a new forward model that is from a similar
 056 distribution as the original forward model, thus consistent with the original inference. This idea has
 057 been used to improve parallel imaging (Zhao & Hu, 2008), then rediscovered in the context of DL
 058 reconstruction training (Kim et al., 2023; Tachella et al., 2022; Zhang et al., 2024) and uncertainty
 059 guidance (Zhang & Akçakaya, 2024). In our work, we use this idea in a completely novel direc-
 060 tion to characterize and mitigate adversarial attacks. Succinctly, without an attack, reconstructions
 061 on synthesized measurements should be cycle-consistent, while with a small adversarial perturba-
 062 tion, there should be large discrepancies between reconstructions from actual versus synthesized
 063 measurements. We use this consistency to devise an objective function over the network input to
 064 effectively mitigate adversarial perturbations. Our contributions are as follows:

- 065 • We propose a novel mitigation strategy for adversarial attacks, which optimizes cyclic measure-
 066 ment consistency over the input within a small ball without requiring *any retraining*.
- 067 • We show that the mitigation strategy can be applied in a manner that is blind to the size of the
 068 perturbation or the algorithm that was used to generate the attack.
- 069 • For the first time, we provide a *realistic* scenario for small adversarial attacks in MRI recon-
 070 struction, related to impulse noise in k-space, associated with herringbone artifacts (Stadler et al.,
 071 2007), as a sparse & bounded adversarial attack. We show our method also mitigates such attacks.
- 072 • Our method readily combines with existing robust training strategies to further improve recon-
 073 struction quality of DL-based MRI reconstruction under adversarial attacks.
- 074 • Our results demonstrate effectiveness across various datasets, PD-DL networks, attack types and
 075 strengths, and undersampling patterns, outperforming existing methods qualitatively and quanti-
 076 tatively, without affecting the performance on non-perturbed images.
- 077 • Finally, we show that the physics-driven nature of our method makes it robust even to adaptive
 078 attacks, where the attacker is aware of the defense strategy and finds the worst-case perturbation
 079 that maximize its effectiveness in bypassing the defense algorithm.

081 2 BACKGROUND AND RELATED WORK

082 2.1 PD-DL RECONSTRUCTION FOR ACCELERATED MRI

085 In MRI, raw measurements are collected in the frequency domain, known as the k-space, using
 086 multiple receiver coils, where each coil is sensitive to different parts of the field-of-view. Accelerated
 087 MRI techniques acquire sub-sampled data, $\mathbf{y}_\Omega = \mathbf{E}_\Omega \mathbf{x} + \mathbf{n}$, where $\mathbf{E}_\Omega \in \mathbb{C}^{M \times N}$ is the forward
 088 multi-coil encoding operator, with $M > N$ in the multi-coil setup (Pruessmann et al., 1999), Ω is
 089 the undersampling pattern with acceleration rate R , \mathbf{n} is measurement noise, and \mathbf{x} is the image to
 090 be reconstructed. The inverse problem for this acquisition model is formulated as

$$091 \arg \min_{\mathbf{x}} \|\mathbf{y}_\Omega - \mathbf{E}_\Omega \mathbf{x}\|_2^2 + \mathcal{R}(\mathbf{x}) \quad (1)$$

093 where the first quadratic term enforces data fidelity (DF) with the measurements, while the sec-
 094 ond term is a regularizer, $\mathcal{R}(\cdot)$. The objective in Eq. (1) is conventionally solved using iterative
 095 algorithms (Fessler, 2020) that alternate between DF and a model-based regularization term.

096 On the other hand, PD-DL commonly employs a technique called algorithm unrolling (Monga et al.,
 097 2021), which unfolds such an iterative reconstruction algorithm for a fixed number of steps. Here,
 098 the DF is implemented using conventional methods with a learnable parameter, while the proximal
 099 operator for the regularizer is implemented implicitly by a neural network (Hammernik et al., 2023).
 100 The unrolled network is trained end-to-end in a supervised manner using fully-sampled reference
 101 data (Hammernik et al., 2018; Aggarwal et al., 2019) using a loss of the form:

$$102 \arg \min_{\theta} \mathbb{E} \left[\mathcal{L}(f(\mathbf{z}_\Omega, \mathbf{E}_\Omega; \theta), \mathbf{x}_{\text{ref}}) \right], \quad (2)$$

105 where $\mathbf{z}_\Omega = \mathbf{E}_\Omega^H \mathbf{y}_\Omega$ is the zero-filled image that is input to the PD-DL network; $f(\cdot, \cdot; \theta)$ is the
 106 output of the PD-DL network, parameterized by θ , in image domain; $\mathcal{L}(\cdot, \cdot)$ is a loss function;
 107 \mathbf{x}_{ref} is the reference image. In this work, we unroll the variable splitting with quadratic penalty
 108 algorithm (Fessler, 2020), as in MoDL (Aggarwal et al., 2019).

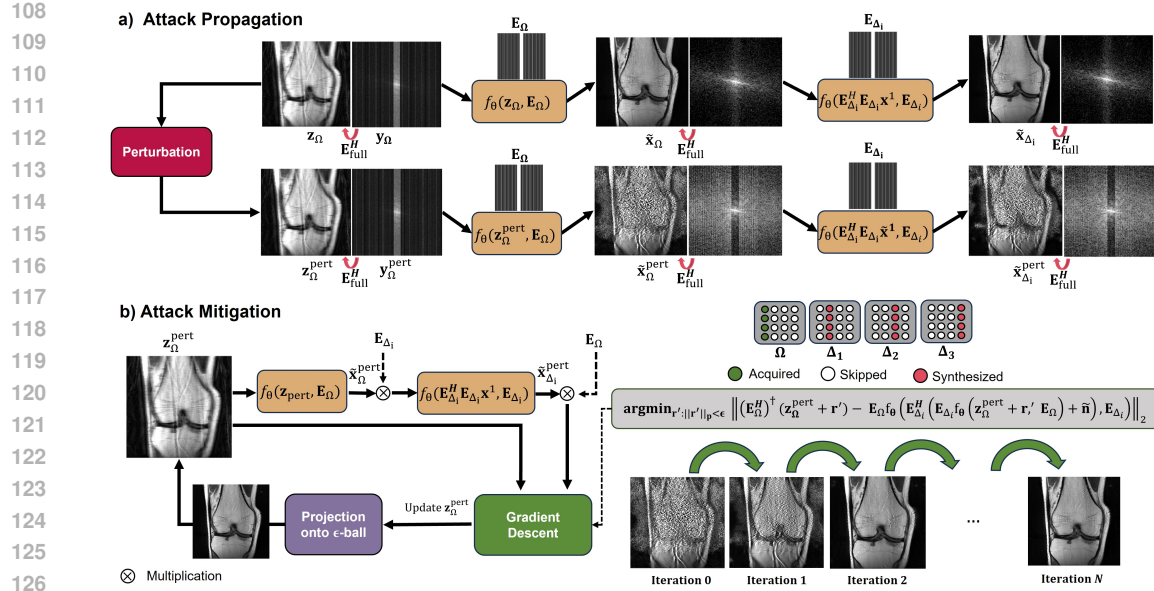


Figure 1: Overview of the proposed mitigation strategy. a) If there is an adversarial attack, the k-space corresponding to the reconstructions of MRI data synthesized from previous DL model outputs will be disrupted. b) This idea is used to devise a novel loss function to find a “corrective” perturbation around the input that ensures cyclic measurement consistency.

2.2 ADVERSARIAL ATTACKS IN PD-DL MRI RECONSTRUCTION

Adversarial attacks create serious challenges for PD-DL MRI reconstruction, where small, visually imperceptible changes to input data can lead to large errors in the reconstructed image (Zhang et al., 2021; Antun et al., 2020; Calivá et al., 2021). These find the worst-case degradation \mathbf{r} within a small ℓ_p ball that will lead to the largest perturbation in the output of the network (Antun et al., 2020):

$$\arg \max_{\mathbf{r}: \|\mathbf{r}\|_p \leq \epsilon} \mathcal{L}(f(\mathbf{z}_\Omega + \mathbf{r}, \mathbf{E}_\Omega; \theta), f(\mathbf{z}_\Omega, \mathbf{E}_\Omega; \theta)). \quad (3)$$

We note that this attack calculation is unsupervised, which is the relevant scenario for MRI reconstruction (Jia et al., 2022; Zhang et al., 2021), as the attacker cannot know the fully-sampled reference for a given undersampled dataset. In MRI reconstruction, ℓ_∞ perturbations are commonly used in image domain (Zhang et al., 2021; Antun et al., 2020; Liang et al., 2023; Jia et al., 2022), while ℓ_2 perturbations are used in k-space (Raj et al., 2020) due to scaling differences between low and high-frequency in Fourier domain. In this work, we concentrate on the former, while examples for the latter are provided in Appendix D.7. We also note that image domain attacks can be converted to k-space as: $\mathbf{w} = (\mathbf{E}_\Omega^H)^\dagger \mathbf{r} = \mathbf{E}_\Omega (\mathbf{E}_\Omega^H \mathbf{E}_\Omega)^{-1} \mathbf{r}$, since $M > N$ for multi-coil MRI acquisitions (Pruessmann et al., 1999). Note \mathbf{w} is only non-zero at Ω , and its zero-filled image is $\mathbf{E}_\Omega^H \mathbf{w} = \mathbf{r}$, as expected. In other words, ℓ_∞ attacks have k-space representations, where only the acquired locations Ω are perturbed, aligning with the underlying physics of the problem.

Adversarial attacks are typically calculated using a gradient-based strategy (Goodfellow et al., 2015; Mkadry et al., 2018), where the input is perturbed in the direction of maximal change within the ℓ_∞ ball. In this study, we use iterative projected gradient descent (PGD) (Mkadry et al., 2018), as it leads to more drastic perturbations than the single-step fast gradient sign method (FGSM) (Goodfellow et al., 2015). Further results with FGSM are included in Appendix D.6. Finally, we note that neural network based attacks have also been used (Raj et al., 2020), but these are mainly preferred for reduced computation time in training, and often fail to match the degradation caused by iterative optimization-based techniques (Jaekle & Kumar, 2021).

2.3 DEFENSE AGAINST ADVERSARIAL ATTACKS IN MRI RECONSTRUCTION

Adversarial training (AT) incorporates an adversarial term in the training objective for robust training, and has been used both in the image domain (Jia et al., 2022) or k-space (Raj et al., 2020). The

162 two common approaches either enforce perturbed outputs to the reference (Jia et al., 2022):
 163

$$164 \min_{\theta} \mathbb{E} \left[\max_{\|\mathbf{r}\|_{\infty} \leq \epsilon} \mathcal{L}[f_{\theta}(\mathbf{z}_{\Omega} + \mathbf{r}, \mathbf{E}_{\Omega}; \theta), \mathbf{x}_{\text{ref}}] \right] \quad (4)$$

166 or aim to balance normal and perturbed training (Raj et al., 2020):
 167

$$168 \min_{\theta} \mathbb{E} \left[\max_{\|\mathbf{r}\|_{\infty} \leq \epsilon} \mathcal{L}[f_{\theta}(\mathbf{z}_{\Omega}, \mathbf{E}_{\Omega}; \theta), \mathbf{x}_{\text{ref}}] + \lambda \mathcal{L}[f_{\theta}(\mathbf{z}_{\Omega} + \mathbf{r}, \mathbf{E}_{\Omega}; \theta), \mathbf{x}_{\text{ref}}] \right], \quad (5)$$

169 where λ is a hyperparameter controlling the trade-off. While such training strategies improve robustness against adversarial attacks, it often comes at the cost of reduced performance on non-perturbed inputs (Tsipras et al., 2019). Another recent method for robust PD-DL reconstruction proposes the idea of smooth unrolling (SMUG) (Liang et al., 2023). SMUG (Liang et al., 2023) modifies denoised smoothing (Salman et al., 2020), introduces robustness to a regularizer part of the unrolled network. Each unrolled unit of SMUG performs:

$$177 \mathbf{x}_s^{(i+1)} = \arg \min_{\mathbf{x}} \|\mathbf{E}_{\Omega} \mathbf{x}_s^{(i)} - \mathbf{y}_{\Omega}\|_2^2 + \lambda \|\mathbf{x} - \mathbb{E}_{\eta}[\mathcal{D}_{\theta}(\mathbf{x}_s^{(i)} + \eta)]\|_2^2 \quad (6)$$

179 where \mathcal{D}_{θ} represents the denoiser network with parameters θ , and $\eta \sim \mathcal{N}(\mathbf{0}, \sigma^2 \mathbf{I})$ is random Gaussian noise. During the training, SMUG (Liang et al., 2023) incorporates P Monte Carlo sampling to smooth the denoiser outputs, averaging them before entering the next DF block.
 180

182 2.4 WHY ARE ADVERSARIAL ATTACKS IMPORTANT IN DL MRI RECONSTRUCTION?

184 **Non-zero probability of worst-case perturbations.** MRI reconstruction pipelines are closed proprietary systems (Winter et al., 2024), thus it is unlikely that an adversary may successfully inject 185 adversarial perturbations during this process. Nonetheless, adversarial attacks provide a *controlled* 186 means to understand the worst-case stability and overall robustness of DL-based reconstruction 187 systems (Antun et al., 2020; Gottschling et al., 2025; Zhang et al., 2021; Han et al., 2024; Alkhouri 188 et al., 2024). It has been argued both empirically (Antun et al., 2020) and theoretically (Gottschling 189 et al., 2025) that worst-case perturbations are not rare events. In particular, if one samples a new 190 input from a small ball around the worst-case perturbation this still leads to a failed reconstruction 191 (Antun et al., 2020). Recent work further shows that sampling from Gaussian noise, i.e. the thermal 192 noise model in MRI, leads to such an instability with non-zero probability (Gottschling et al., 2025).
 193

194 **Connection to herringbone artifacts.** Apart from Gaussian noise, there are several other causes 195 of perturbations in an MRI scan, including body motion (Zaitsev et al., 2015) or hardware issues 196 (Kashani et al., 2020), which are hard to model mathematically in general, but whose combined 197 effect may lead to similar instabilities for DL-based reconstruction (Antun et al., 2020). One such 198 hardware-related issue is electromagnetic spikes from the gradient power fluctuation or inadequate 199 room shielding, resulting in impulse noise in k-space, which manifest as herringbone artifacts in 200 image domain (Stadler et al., 2007; Jin et al., 2017). When the impulse intensities are high, these 201 artifacts are visible even in fully-sampled data. However, lower intensity impulses may adversely 202 affect DL reconstruction. For the first time, we show this using a sparse and bounded attack model.
 203

204 **Understanding broader perturbations.** Adversarial perturbations and mitigation algorithms, like 205 ours, are critical to understand the robustness of DL reconstruction models in important scenarios, 206 such as performance for rare pathologies (Muckley et al., 2021). However, these physiological 207 changes are much harder to model and simulate, unlike adversarial attacks, which provide insights 208 into worst-case stability. Finally, we note that our mitigation algorithm is also applicable to unrolled 209 networks in general, and may have applications in broader computational imaging scenarios.
 210

211 3 PROPOSED METHOD FOR TRAINING-FREE MITIGATION OF ADVERSARIAL 212 ATTACKS IN PD-DL MRI

213 3.1 ATTACK PROPAGATION IN SIMULATED K-SPACE

214 The idea behind our mitigation strategy stems from cyclic measurement consistency with synthesized
 215 undersampling patterns, which has been previously used to improve calibration/training of

MRI reconstruction models (Zhao & Hu, 2008; Kim et al., 2023; Tachella et al., 2022; Zhang & Akçakaya, 2024; Zhang et al., 2024). For reconstruction purposes, a well-trained model should generalize to undersampling patterns with similar distributions as the acquisition one (Knoll et al., 2020a). To this end, let $\{\Delta_n\}$ be undersampling patterns drawn from a similar distribution as Ω , including same acceleration rate, similar underlying distribution, e.g. variable density random, and same number of central lines. Further let

$$\tilde{\mathbf{x}}_\Omega = f(\mathbf{z}_\Omega, \mathbf{E}_\Omega; \theta) \quad (7)$$

be the reconstruction of the acquired data. We simulate new measurements $\tilde{\mathbf{y}}_{\Delta_i}$ from $\tilde{\mathbf{x}}$ using the encoding operator \mathbf{E}_{Δ_i} with the same coil sensitivity profiles as \mathbf{E}_Ω , and let $\mathbf{z}_{\Delta_i} = \mathbf{E}_{\Delta_i}^H \tilde{\mathbf{y}}_{\Delta_i}$ be the corresponding zerofilled image. Then the subsequent reconstruction

$$\tilde{\mathbf{x}}_{\Delta_i} = f(\mathbf{z}_{\Delta_i}, \mathbf{E}_{\Delta_i}; \theta) \quad (8)$$

should be similar to $\tilde{\mathbf{x}}_\Omega$. In particular, we evaluate the similarity over the acquired k-space locations, Ω , as we will discuss in Section 3.2. However, if there is an attack on the acquired lines, either generated directly in k-space or in image domain as discussed in Section 2.2, then this consistency with synthesized measurements are no longer expected to hold, as illustrated in Fig. 1a.

This can be understood in terms of what the PD-DL network does during reconstruction as it alternates between DF and regularization. The DF operation will ensure that the network is consistent with the input measurements, \mathbf{y}_Ω , or equivalently the zerofilled image, \mathbf{z}_Ω . If there is no adversarial attack, we expect the output of a well-trained PD-DL network to be consistent with these measurements, while also showing no sudden changes in k-space (Knoll et al., 2020a). On the other hand, if there is an attack, the output will still be consistent with the measurements, as the attack is designed to be a small perturbation on \mathbf{y}_Ω or \mathbf{z}_Ω , and thus the small changes on these lines will be imperceptible. Instead, the attack will affect all the other k-space locations Ω^C , the complement of the acquired index set, leading to major changes in these lines for the output of the PD-DL network, as depicted in Fig. 1a. Thus, when we resample a new set of indices Δ_i that includes lines from Ω^C , under attack the next level reconstruction $\tilde{\mathbf{x}}_{\Delta_i}$ will no longer be consistent with the original k-space data \mathbf{y}_Ω , as measured through $\|\mathbf{y}_\Omega - \mathbf{E}_\Omega \tilde{\mathbf{x}}_{\Delta_i}\|_2$. The distortion in the k-space will further propagate as we synthesize more levels of data and reconstruct these, if there is an adversarial attack. The following theorem further confirms this intuition:

Theorem 1. *Let \mathbf{y}_Ω and $\tilde{\mathbf{y}}_\Omega = \mathbf{y}_\Omega + \mathbf{w}$ be the clean and perturbed measurements, respectively, and let \mathbf{x} and $\tilde{\mathbf{x}}$ denote the corresponding outputs of the PD-DL network. Then*

$$\|\mathbf{E}_\Omega(\tilde{\mathbf{x}} - \mathbf{x})\|_2 \leq C\|\mathbf{w}\|_2, \quad (9)$$

where C is a function of the smallest and largest singular values of \mathbf{E}_Ω and \mathbf{E}_{Ω^C} , a constant characterizing the high-frequency energy of the smooth coil sensitivity maps, the learned DF penalty parameter in MoDL, the number of unrolls, and the Lipschitz constant of the proximal network.

Proof and details on the constants, are given in Appendix G. Since $\|\tilde{\mathbf{x}} - \mathbf{x}\|_2^2 = \|\mathbf{E}_\Omega(\tilde{\mathbf{x}} - \mathbf{x})\|_2^2 + \|\mathbf{E}_{\Omega^C}(\tilde{\mathbf{x}} - \mathbf{x})\|_2^2$, the theorem implies the residual error on the complementary set Ω^C must be large.

This description of the attack propagation suggests a methodology for detecting such attacks; however, this is not the focus of this paper. As discussed in Appendix D.4, mitigation can be applied on all inputs, regardless of whether they have been attacked, as the algorithm does not degrade the reconstruction if the input is unperturbed. Thus, to keep the exposition clearer, we focus on mitigation for the remainder of the paper, and a threshold-based detection scheme is discussed in Appendix C.

3.2 ATTACK MITIGATION WITH CYCLIC CONSISTENCY

Based on the characterization of the attack propagation, we next introduce our proposed training-free mitigation strategy. We note that adversarial attacks of Section 2.2 all aim to create a small perturbation within a ball around the original input. Here the size of the ball specifies the attack strength, the particular algorithm specifies how the attack is generated within the given ball, and the attack domain/norm specifies the type of ℓ_p ball and whether it is in k-space or image domain.

Succinctly, our mitigation approach aims to reverse the attack generation process, by searching within a small ball around the perturbed input to find a clear input. The objective function for this

270 task uses the aforementioned idea of cyclic measurement consistency, and is given as
 271

$$272 \arg \min_{\mathbf{r}' : \|\mathbf{r}'\|_p \leq \epsilon} \mathbb{E}_{\Delta} \left[\left\| (\mathbf{E}_{\Omega}^H)^{\dagger} (\mathbf{z}_{\Omega} + \mathbf{r}') - \mathbf{E}_{\Omega} f \left(\mathbf{E}_{\Delta}^H (\mathbf{E}_{\Delta} f(\mathbf{z}_{\Omega} + \mathbf{r}', \mathbf{E}_{\Omega}; \theta) + \tilde{\mathbf{n}}), \mathbf{E}_{\Delta}; \theta \right) \right\|_2 \right], \quad (10)$$

275 where \mathbf{r}' is a small “corrective” perturbation and $\mathbf{z}_{\Omega} + \mathbf{r}'$ corresponds to the mitigated/corrected input.
 276 The first term, $(\mathbf{E}_{\Omega}^H)^{\dagger} (\mathbf{z}_{\Omega} + \mathbf{r}')$ is the minimum ℓ_2 k-space solution that maps to this zero-filled image
 277 (Zhang et al., 2021). The second term is the corresponding k-space values at the acquired indices Ω
 278 after two stages of cyclic reconstruction. Note a small noise term, $\tilde{\mathbf{n}}$, is added to the synthesized data
 279 to maintain similar signal-to-noise-ratio (Zhang et al., 2024; Knoll et al., 2019). The expectation is
 280 taken over undersampling patterns Δ with a similar distribution to the original pattern Ω .

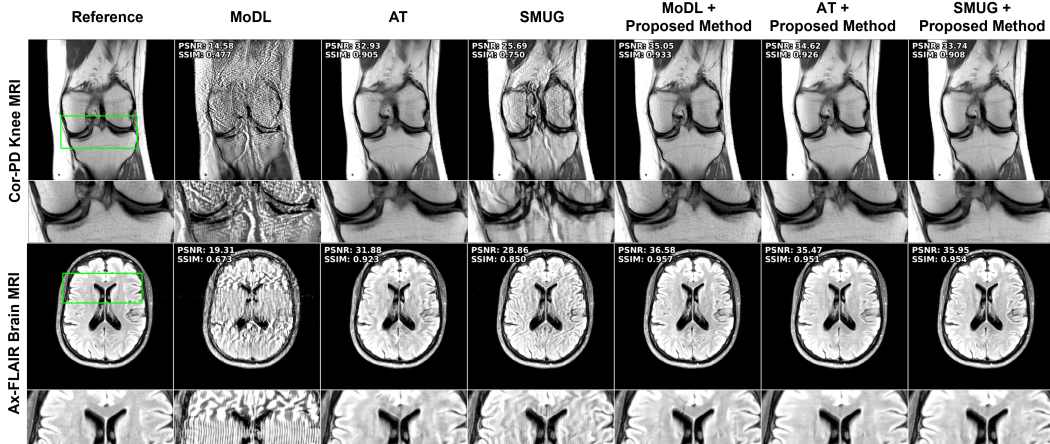
281 The objective function is solved using a reverse PGD approach, as detailed in Algorithm 1. Note
 282 the algorithm performs the expectation in Eq. (10) over K sampling pattern $\{\Delta_k\}_{k=1}^K$. Notably, our
 283 reverse PGD performs a gradient descent instead of the ascent in PGD (Mkadry et al., 2018), and
 284 includes a projection on to the ϵ ball to ensure the solution remains within the desired neighborhood.
 285

286 Finally, this algorithm uses the
 287 strength of the attack, but it is practi-
 288 cally beneficial to mitigate the attack
 289 without it, as this will not always be
 290 available to the end user. In this blind
 291 setup, we additionally optimize its in-
 292 put parameters ϵ and α jointly with
 293 Eq. (10) in an iterative manner. First,
 294 we decrease ϵ with a linear scheduler
 295 for a fixed α , starting from a large ball
 296 until convergence. Subsequently, we
 297 fix ϵ and decrease α similarly. The
 298 alternating process can be repeated,
 299 though in practice, one stage is suf-
 300 ficient. Finally, for blind mitigation,
 301 we always use ℓ_{∞} ball, even for ℓ_2
 302 attacks in k-space discussed in Ap-
 303 pendix E, as it contains the ℓ_2 ball of
 304 the same radius.
 305

Algorithm 1 Attack Mitigation

Require: $\epsilon, \alpha, \mathbf{z}_{\Omega}^{pert}, \mathbf{E}_{\Omega}, \{\mathbf{E}_{\Delta_k}\}_{k=1}^K, f(\cdot, \cdot; \theta)$ \triangleright Inputs
Ensure: Clean version of $\mathbf{z}_{\Omega}^{pert}$ \triangleright Mitigate attack on input

- 1: $\tilde{\mathbf{z}}_{\Omega} = \mathbf{z}_{\Omega}^{pert}$
- 2: **repeat**
- 3: Loss = 0
- 4: **for** $k = 1$ to K **do**
- 5: $\tilde{\mathbf{y}}_{\Omega} = (\mathbf{E}_{\Omega}^H)^{\dagger} \tilde{\mathbf{z}}_{\Omega}$
- 6: $\tilde{\mathbf{y}}_{\Omega} = \mathbf{E}_{\Omega} f \left(\mathbf{E}_{\Delta_k}^H (\mathbf{E}_{\Delta_k} f(\tilde{\mathbf{z}}_{\Omega}, \mathbf{E}_{\Omega}; \theta) + \tilde{\mathbf{n}}), \mathbf{E}_{\Delta_k}; \theta \right)$
- 7: $loss_k = \|\tilde{\mathbf{y}}_{\Omega} - \tilde{\mathbf{y}}_{\Omega}\|_2$ \triangleright Eq. 10
- 8: Loss = Loss + $loss_k$
- 9: **end for**
- 10: grad = $\frac{1}{K} \nabla_{\tilde{\mathbf{z}}_{\Omega}} \text{Loss}$
- 11: $\tilde{\mathbf{z}}_{\Omega} = \tilde{\mathbf{z}}_{\Omega} - \alpha \cdot \text{sgn}(\text{grad})$
- 12: $\tilde{\mathbf{z}}_{\Omega} = \text{clip}_{\mathbf{z}_{\Omega}^{pert}, \epsilon}(\tilde{\mathbf{z}}_{\Omega})$ \triangleright Projection to ϵ ball
- 13: **until** Converge



320 Figure 2: Representative reconstruction results for Cor-PD knee, and Ax-FLAIR brain MRI Datasets
 321 at $R = 4$. The attack inputs lead to severe disruption in the baseline MoDL reconstruction. Adver-
 322 sarial training improves these, albeit suffering from blurriness. SMUG fails to eliminate the attack.
 323 The proposed strategy reduces the artifacts and maintains sharpness. Furthermore it can be com-
 bined with the other strategies for further gains (last two columns).

324 3.3 MITIGATION PERFORMANCE ON ADAPTIVE ATTACKS
325

326 Recent works suggest that a good performance on iterative optimization-based attacks may not be a
327 good indicator of robustness, as the class of adaptive attacks can jointly deceive the baseline (recon-
328 struction) network and bypass the defense once the attacker is aware of the defense strategy (Carlini
329 & Wagner, 2017). Consequently, they have become the standard when evaluating defenses (Tramer
330 et al., 2020). To generate adaptive attacks, our mitigation in Algorithm 1 needs to be incorporated
331 into the attack generation objective Eq. (3). To simplify the notation, we define our mitigation
332 function based on Eq. (10) as

$$333 \quad g(\mathbf{z}_\Omega) \triangleq \min_{\mathbf{r}': \|\mathbf{r}'\|_p \leq \epsilon} \mathbb{E}_\Delta \left[\left\| (\mathbf{E}_\Omega^H)^\dagger (\mathbf{z}_\Omega + \mathbf{r}') - \mathbf{E}_\Omega f \left(\mathbf{E}_\Delta^H (\mathbf{E}_\Delta f(\mathbf{z}_\Omega + \mathbf{r}', \mathbf{E}_\Omega; \theta) + \tilde{\mathbf{n}}), \mathbf{E}_\Delta; \theta \right) \right\|_2 \right]$$

335 which leads to the adaptive attack generation objective:

$$336 \quad \arg \max_{\mathbf{r}: \|\mathbf{r}\|_p \leq \epsilon} \mathcal{L}(f(\mathbf{z}_\Omega + \mathbf{r}, \mathbf{E}_\Omega; \theta), f(\mathbf{z}_\Omega, \mathbf{E}_\Omega; \theta)) + \lambda g(\mathbf{z}_\Omega + \mathbf{r}), \quad (11)$$

338 where the first term finds a perturbation that fools the baseline, as in Eq. (3), while the second term
339 integrates our mitigation. Thus, maximizing Eq. (11) leads to a perturbation \mathbf{r} that not only misleads
340 the baseline reconstruction, but also maximizes the mitigation loss, resulting in an adaptive attack.
341

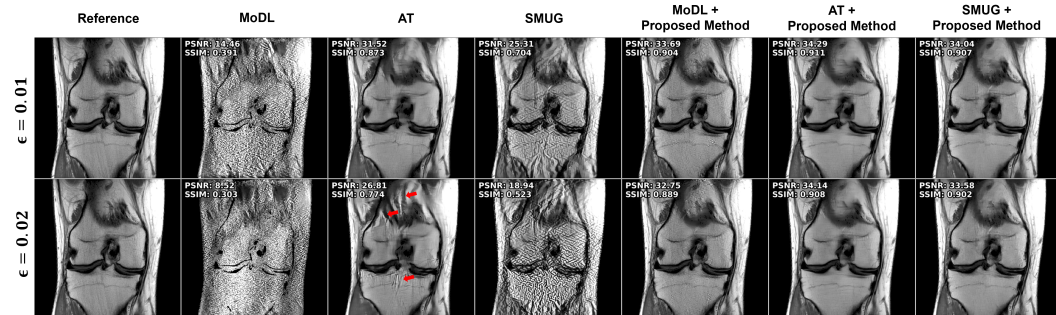
342 4 EXPERIMENTS
343344 4.1 IMPLEMENTATION DETAILS
345

346 **Datasets.** Multi-coil coronal proton density (Cor-PD) knee and axial FLAIR (Ax-FLAIR) brain
347 MRI from fastMRI database (Knoll et al., 2020b), respectively with 15 and 20 coils, were used.
348 Retrospective equispaced undersampling was applied at acceleration $R = 4$ to the fully-sampled
349 data with 24 central auto-calibrated signal (ACS) lines.

350 **Baseline Network.** The PD-DL network used in this study was a modified version of MoDL
351 (Aggarwal et al., 2019), unrolled for 10 steps, where a ResNet regularizer was used (Yaman et al.,
352 2022b). Further details about the architecture and training are provided in Appendix A. All compar-
353 ison methods were implemented using this MoDL network to ensure a fair comparison, except for
354 the results on the applicability of our method to different PD-DL networks.

355 **Attack Generation Details.** PGD (Mkadry et al., 2018) was used to generate the attacks in an un-
356 supervised manner, as detailed earlier for a realistic setup. Additional results with supervised attacks
357 and FGSM are provided in Appendix D.5 and D.6, respectively, and lead to the same conclusions.
358 Complex images were employed to generate the attack and gradients, and MSE loss was used.
359

360 **Comparison Methods.** We compared our mitigation approach with existing robust training meth-
361 ods, including adversarial training (Jia et al., 2022; Raj et al., 2020) and Smooth Unrolling
362 (SMUG) (Liang et al., 2023). Adversarial training was implemented using Eq. (4) (Jia et al., 2022),
363 while results using Eq. (5) (Raj et al., 2020) is provided in Appendix D.3. Further implementation
364 details for all methods are provided in Appendix A.



376 Figure 3: Performance across different attack strengths. Both Adversarial Training and SMUG fail
377 to perform well against attack strengths they were not trained on. In contrast, the proposed training-
378 free mitigation shows good performance across perturbation levels.

378 **Cyclic Consistency Details.** The synthesized masks $\{\Delta_k\}$ were generated by shifting the equi-
 379 spaced undersampling patterns by one line while preserving the ACS lines (Zhang et al., 2024). In
 380 this setting, the number of synthesized masks is $R - 1$.
 381

382 **Adaptive Attack Details.** Direct optimization of Eq. (11) requires the solution of a long compu-
 383 tation graph and multiple nested iterations of neural networks. However, this may induce gradient
 384 obfuscation, leading to a false sense of defense security (Athalye et al., 2018). Thus, we followed
 385 the gradient computation strategy of (Chen et al., 2023), by unrolling $g(\cdot)$ in Eq. (11) first (Yang
 386 et al., 2022), and then backpropagating through the whole objective. Hence, we let $g_T(\cdot)$ be the T -
 387 step unrolled version of $g(\cdot)$, and report performance for different T . Additional information about
 388 checkpointing for large T , tuning of λ and noise precalculation for \hat{n} are provided in Appendix F.
 389

390 4.2 ATTACK MITIGATION RESULTS

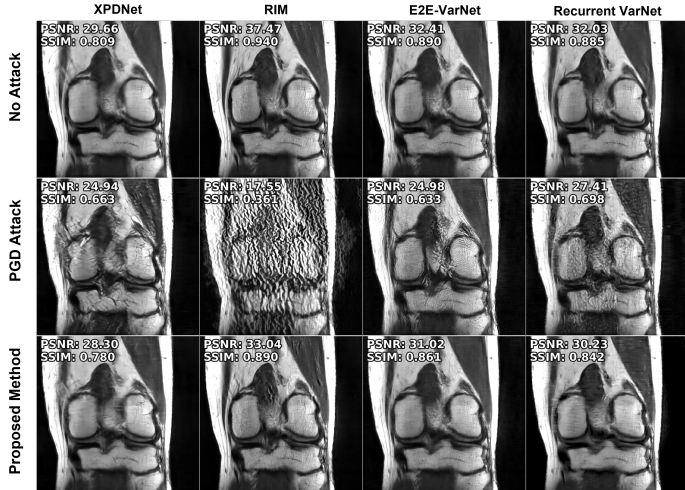
392 **Performance Across Datasets.** We first study our approach and the comparison methods on knee
 393 and brain MRI datasets at $R = 4$. Fig. 2 shows that baseline PD-DL (MoDL) has substantial
 394 artifacts under attack. SMUG improves these but still suffers from noticeable artifacts. AT re-
 395 solves the artifacts, albeit with blurring. Our proposed approach successfully mitigates the attacks
 396 *without any retraining*, while main-
 397 taining sharpness. We note our
 398 method can also be combined with
 399 SMUG and AT to further improve
 400 performance. Tab. 1 summarizes the
 401 quantitative metrics for all test slices,
 402 consistent with visual observations.

403 **Performance Across Attack Strengths and Blind Mitigation.** We next test the meth-
 404 ods across different attack strengths, $\epsilon \in \{0.01, 0.02\}$. Fig. 3 shows the results for both
 405 attack strengths using the robust training methods trained with $\epsilon = 0.01$ and proposed miti-
 406 gation. As in Fig. 2, SMUG has artifacts at $\epsilon = 0.01$, which gets worse at $\epsilon = 0.02$.
 407 Similarly, AT struggles at $\epsilon = 0.02$, since it was trained at $\epsilon = 0.01$, leading to visible
 408 artifacts (arrows). On the other hand, our training-free mitigation is successful at both ϵ .
 409 This is expected, since no
 410 matter how big the ϵ ball is,
 411 our mitigation explores the
 412 corresponding vicinity of the
 413 perturbed sample to optimize
 414 Eq. (10). Further quantitative
 415 results are in Appendix D.1.
 416 Implementation details and
 417 results on blind mitigation
 418 without knowledge of attack
 419 type/strength are in Appendix E.

420 **Performance Across Different**
 421 **PD-DL Networks.** Next, we
 422 hypothesize that our method is
 423 agnostic to the PD-DL architec-
 424 ture. To test this hypothesis, we
 425 perform our mitigation approach
 426 for different unrolled networks,
 427 including XPDNet (Ramzi et al.,
 428 2020), Recurrent Inference Ma-
 429 chine (Lønning et al., 2019), E2E-VarNet (Sriram et al., 2020), and Recurrent-VarNet (Yiasemis
 430 et al., 2022b). The implementation details are discussed in Appendix A.1. Fig. 4 depicts rep-
 431 resentative images for clear and perturbed inputs, and our proposed cyclic mitigation results. Overall, all
 432 networks show artifacts for perturbed inputs, while our proposed cyclic mitigation algorithm works
 433 well on all of them to reduce these artifacts. Further quantitative metrics for these networks are in
 434 Appendix D.2.

391 Table 1: SSIM/PSNR on all test slices.

Dataset	Metric	SMUG	Adversarial Training (AT)	Proposed Method + MoDL / SMUG / AT
Cor-PD	PSNR	28.22	33.99	35.14 / 34.85 / 36.57
	SSIM	0.79	0.92	0.92 / 0.92 / 0.94
Ax-FLAIR	PSNR	29.67	34.03	36.41 / 34.67 / 35.63
	SSIM	0.84	0.91	0.95 / 0.92 / 0.94



435 Figure 4: Proposed mitigation approach is readily applicable to
 436 various PD-DL networks for MRI reconstruction.

432
Performance Against Herringbone
 433 **Artifacts.** Next, we assess the miti-
 434 gation algorithm against an ℓ_0 attack,
 435 simulating small spikes in k-space,
 436 which may occur due to hardware is-
 437 sues (Stadler et al., 2007). Fig. 5
 438 shows how a few small spikes can
 439 lead to instabilities in MoDL, simi-
 440 lar to herringbone artifacts. Our miti-
 441 gation effectively removes these. Fur-
 442 ther implementation details and quantita-
 443 tive results are provided in the Appendix B.

443 **Performance Against Adaptive Attacks.**

444 Tab. 2 shows the performance of our miti-
 445 gation algorithm for adaptive attacks with
 446 $T \in \{10, 25, 50, 100\}$ unrolls. Due to
 447 the high computational cost of generating
 448 adaptive attacks for $T = 100$, we ran the
 449 adaptive attack mitigation on a subset of
 450 75 Cor-PD slices, which is why the non-
 451 adaptive attack results have lower PSNR
 452 than the full test set in Tab. 1. For mitigation of adaptive attacks, we ran both an unrolled version
 453 (used to generate the adaptive attack) and an iterative version (ran until convergence) of Algorithm 1.
 454 Average number of iterations for the latter are reported in parenthesis in the last column. Further
 455 visual examples are in Appendix F. We observe the following: 1) Baseline reconstructions have higher
 456 PSNR under adaptive attacks than non-adaptive attacks, as adaptive attacks balance two terms, re-
 457 ducing its focus on purely destroying the reconstruction. This effect increases as T increases, as
 458 expected. 2) For few number of unrolls, adaptive attack degrades performance if mitigated with the
 459 unrolled version. For $T < 50$, the unrolled mitigation struggles (~ 5 dB degradation for $T = 10$)
 460 with the adaptive attack designed for matched number of unrolls. 3) Our mitigation readily resolves
 461 adaptive attacks if run until convergence. For large $T \geq 50$, unrolled mitigation also largely resolves
 462 adaptive attacks. 4) Even though adaptive attacks with large T lead to a weaker baseline attack, they
 463 degrade our mitigation more, even though the overall degradation is slight even at $T = 100$ (.68dB).

464 These observations all align with the physics-driven design of the mitigation: The PD-DL recon-
 465 struction network ends with data fidelity, i.e. the network output is consistent with (perturbed) \mathbf{y}_Ω .
 466 Since the attack is a tiny perturbation on data at Ω , it will cause misestimation of lines in Ω^C instead
 467 (as in Fig. 1a and Theorem 1). Our method synthesizes new measurements at Δ from the latter, and
 468 uses it to perform a second reconstruction, which are mapped to Ω and checked for consistency with
 469 \mathbf{y}_Ω . Thus, the only way the mitigation can be fooled is if this cyclic consistency is satisfied, which
 470 in turn indicates that the intermediate recon on Ω^C is good, effectively mitigating the attack.

470 4.3 ABLATION STUDY

471 We perform an ablation study on how many levels of reconstructions are needed for mitigation. In
 472 this case, multiple steps of reconstructions and data synthesis can be used to update the loss function
 473 in Eq. (10). Results, given in Appendix H, show that enforcing cyclic consistency with multiple
 474 levels degrades performance and requires more computational resources. Hence, using 2-cyclic
 475 reconstruction stages is the best choice from both performance and computational perspectives.

477 5 CONCLUSIONS

478 In this study, we proposed a method to mitigate small imperceptible adversarial input perturbations
 479 on DL MRI reconstructions, without requiring any retraining. We showed our method is robust
 480 across different datasets, networks, attack strengths/types, including the practical herringbone attack.
 481 Our method can be combined with existing robust training methods to further enhance their per-
 482 formance. Additionally, our technique can be performed in a blind manner without attack-specific
 483 information, such as attack strength or type. Finally, owing to its physics-based design, our method
 484 is robust to adaptive attacks, which have emerged as the recent standard for robustness evaluation.

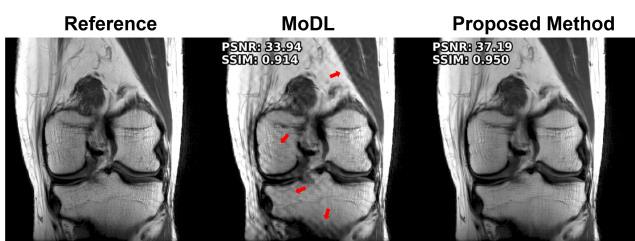


Figure 5: Mitigation of a herringbone (ℓ_0) perturbation.
 Further implementation details and quantitative results are provided in the Appendix B.

Table 2: PSNR for adaptive attacks on 75 Cor-PD slices. Parentheses in the last column indicate the mean iteration for convergence of the iterative algorithm.

Attack Type	#Unrolls (T)	Baseline Reconstruction	Unrolled Algorithm 1	Iterative Algorithm 1
Non-adaptive	N/A	16.16	N/A	34.69
Adaptive	10	19.23	29.47	34.34 (119 iters)
Adaptive	25	19.32	32.79	34.16 (111 iters)
Adaptive	50	19.96	33.39	34.14 (105 iters)
Adaptive	100	21.02	33.78	34.01 (100 iters)

486 REFERENCES
487

488 Jonas Adler and Ozan Öktem. Learned primal-dual reconstruction. *IEEE Trans Med Imaging*, 37
489 (6):1322–1332, 2018.

490 Hemant K Aggarwal, Merry P Mani, and Mathews Jacob. MoDL: Model-based deep learning
491 architecture for inverse problems. *IEEE Trans Med Imaging*, 38(2):394–405, Feb 2019.

492 Mehmet Akçakaya, Burhaneddin Yaman, Hyungjin Chung, and Jong Chul Ye. Unsupervised deep
493 learning methods for biological image reconstruction and enhancement: An overview from a
494 signal processing perspective. *IEEE Sig Proc Mag.*, 39(2):28–44, March 2022.

495 Ismail Alkhouri, Shijun Liang, Rongrong Wang, Qing Qu, and Saiprasad Ravishankar. Ro-
496 bust physics-based deep mri reconstruction via diffusion purification. *arXiv preprint*
497 *arXiv:2309.05794*, 2023.

498 Ismail Alkhouri, Shijun Liang, Rongrong Wang, Qing Qu, and Saiprasad Ravishankar. Diffusion-
499 based adversarial purification for robust deep MRI reconstruction. In *2024 IEEE ICASSP*, pp.
500 12841–12845. IEEE, 2024.

501 Vegard Antun, Francesco Renna, Clarice Poon, Ben Adcock, and Anders C Hansen. On instabilities
502 of deep learning in image reconstruction and the potential costs of AI. *Proceedings of the National*
503 *Academy of Sciences*, 117(48):30088–30095, 2020.

504 Anish Athalye, Nicholas Carlini, and David Wagner. Obfuscated gradients give a false sense of
505 security: Circumventing defenses to adversarial examples. In *ICLR*, pp. 274–283. PMLR, 2018.

506 Ayse Elvan Aydemir, Alptekin Temizel, and Tugba Taskaya Temizel. The effects of jpeg and
507 jpeg2000 compression on attacks using adversarial examples. *arXiv preprint arXiv:1803.10418*,
508 2018.

509 Jacob Buckman, Aurko Roy, Colin Raffel, and Ian Goodfellow. Thermometer encoding: One hot
510 way to resist adversarial examples. In *ICLR*, 2018.

511 Emre Cakir, Giambattista Parascandolo, Toni Heittola, Heikki Huttunen, and Tuomas Virtanen. Con-
512 volutional recurrent neural networks for polyphonic sound event detection. *IEEE/ACM Transac-
513 tions on Audio, Speech, and Language Processing*, 25(6):1291–1303, 2017.

514 Francesco Calivá, Kaiyang Cheng, Rutwik Shah, and Valentina Pedoia. Adversarial robust training
515 of deep learning MRI reconstruction models. *MELBA*, 2021.

516 Nicholas Carlini and David Wagner. Adversarial examples are not easily detected: Bypassing ten de-
517 tection methods. In *Proceedings of the 10th ACM workshop on artificial intelligence and security*,
518 pp. 3–14, 2017.

519 Antonin Chambolle and Thomas Pock. A first-order primal-dual algorithm for convex problems
520 with applications to imaging. *J Math Imaging Vis*, 40:120–145, 2011.

521 Chong Chen, Yingmin Liu, Philip Schniter, Matthew Tong, Karolina Zareba, Orlando Simonetti,
522 Lee Potter, and Rizwan Ahmad. Ocmr (v1. 0)—open-access multi-coil k-space dataset for cardio-
523 vascular magnetic resonance imaging. *arXiv preprint arXiv:2008.03410*, 2020.

524 Huanran Chen, Yinpeng Dong, Zhengyi Wang, Xiao Yang, Chengqi Duan, Hang Su, and Jun Zhu.
525 Robust classification via a single diffusion model. *arXiv preprint arXiv:2305.15241*, 2023.

526 Kaiyang Cheng, Francesco Calivá, Rutwik Shah, Misung Han, Sharmila Majumdar, and Valentina
527 Pedoia. Addressing the false negative problem of deep learning MRI reconstruction models by
528 adversarial attacks and robust training. In *Medical Imaging with Deep Learning*, pp. 121–135.
529 PMLR, 2020.

530 Kyunghyun Cho. Learning phrase representations using RNN encoder-decoder for statistical ma-
531 chine translation. *arXiv preprint arXiv:1406.1078*, 2014.

532 Hyungjin Chung and Jong Chul Ye. Score-based diffusion models for accelerated mri. *Medical*
533 *image analysis*, 80:102479, 2022.

540 Jeremy Cohen, Elan Rosenfeld, and Zico Kolter. Certified adversarial robustness via randomized
 541 smoothing. In *international conference on machine learning*, pp. 1310–1320. PMLR, 2019.
 542

543 Adelina-Valentina Cucu, Giuseppe Valenzise, Daniela Stănescu, Ioana Ghergulescu, Lucian Ionel
 544 Găină, and Bianca Gușă. Defense method against adversarial attacks using jpeg compression
 545 and one-pixel attack for improved dataset security. In *2023 27th International Conference on
 546 System Theory, Control and Computing (ICSTCC)*, pp. 523–527. IEEE, 2023.

547 Omer Burak Demirel, Burhaneddin Yaman, Chetan Shenoy, Steen Moeller, Sebastian Weingärtner,
 548 and Mehmet Akçakaya. Signal intensity informed multi-coil encoding operator for physics-
 549 guided deep learning reconstruction of highly accelerated myocardial perfusion cmr. *Magn Reson
 550 Med*, 89(1):308–321, 2023a.

551 Omer Burak Demirel, Burhaneddin Yaman, Chetan Shenoy, Steen Moeller, Sebastian Weingärtner,
 552 and Mehmet Akçakaya. Signal intensity informed multi-coil encoding operator for physics-
 553 guided deep learning reconstruction of highly accelerated myocardial perfusion cmr. *Magn Reson
 554 Med*, 89(1):308–321, 2023b.

555 Jeffrey A Fessler. Optimization methods for magnetic resonance image reconstruction: Key models
 556 and optimization algorithms. *IEEE Sig Proc Mag*, 37(1):33–40, Jan 2020.

557 Ian J Goodfellow, Jonathon Shlens, and Christian Szegedy. Explaining and harnessing adversarial
 558 examples. *ICLR*, 2015.

559 Nina M Gottschling, Vegard Antun, Anders C Hansen, and Ben Adcock. The troublesome kernel:
 560 On hallucinations, no free lunches, and the accuracy-stability tradeoff in inverse problems. *SIAM
 561 Review*, 67(1):73–104, 2025.

562 Chuan Guo, Mayank Rana, Moustapha Cisse, and Laurens Van Der Maaten. Countering adversarial
 563 images using input transformations. *arXiv preprint arXiv:1711.00117*, 2017.

564 Kerstin Hammernik, Teresa Klatzer, Erich Kobler, Michael P Recht, Daniel K Sodickson, Thomas
 565 Pock, and Florian Knoll. Learning a variational network for reconstruction of accelerated MRI
 566 data. *Magn Reson Med*, 79:3055–3071, Jun 2018.

567 Kerstin Hammernik, Thomas Küstner, Burhaneddin Yaman, Zhengnan Huang, Daniel Rueckert,
 568 Florian Knoll, and Mehmet Akçakaya. Physics-driven deep learning for computational magnetic
 569 resonance imaging: Combining physics and machine learning for improved medical imaging.
 570 *IEEE Sig Proc Mag*, 40(1):98–114, 2023.

571 Tianyu Han, Sven Nebelung, Firas Khader, Jakob Nikolas Kather, and Daniel Truhn. On instabilities
 572 of unsupervised denoising diffusion models in magnetic resonance imaging reconstruction. In
 573 *International Conference on Medical Image Computing and Computer-Assisted Intervention*, pp.
 574 509–517. Springer, 2024.

575 Seyed Amir Hossein Hosseini, Burhaneddin Yaman, Steen Moeller, Mingyi Hong, and Mehmet
 576 Akçakaya. Dense recurrent neural networks for accelerated MRI: History-cognizant unrolling of
 577 optimization algorithms. *IEEE Journal of Selected Topics in Signal Processing*, 14(6):1280–1291,
 578 2020.

579 Florian Jaeckle and M Pawan Kumar. Generating adversarial examples with graph neural networks.
 580 In *Uncertainty in Artificial Intelligence*, pp. 1556–1564. PMLR, 2021.

581 Jinghan Jia, Mingyi Hong, Yimeng Zhang, Mehmet Akçakaya, and Sijia Liu. On the robustness
 582 of deep learning-based MRI reconstruction to image transformations. *NeurIPS 2022 Workshop*,
 583 2022.

584 Kyong Hwan Jin, Ji-Yong Um, Dongwook Lee, Juyoung Lee, Sung-Hong Park, and Jong Chul Ye.
 585 MRI artifact correction using sparse+ low-rank decomposition of annihilating filter-based hankel
 586 matrix. *Magn Reson Med*, 78(1):327–340, 2017.

587 Hong Jung, Kyunghyun Sung, Krishna S Nayak, Eung Yeop Kim, and Jong Chul Ye. k-t focuss: a
 588 general compressed sensing framework for high resolution dynamic MRI. *Magn Reson Med*, 61
 589 (1):103–116, 2009.

594 Tero Karras, Timo Aila, Samuli Laine, and Jaakko Lehtinen. Progressive growing of gans for im-
 595 proved quality, stability, and variation. *arXiv preprint arXiv:1710.10196*, 2017.

596

597 Nima. Kashani, Mohammed Nazir. Khan, Johanna. Ospel, and Xing-Chang. Wei. MRI head coil
 598 malfunction producing artifacts mimicking malformation of cortical development in pediatric
 599 epilepsy work-up. *American Journal of Neuroradiology*, 41(8):1538–1540, 2020. ISSN 0195-
 600 6108. doi: 10.3174/ajnr.A6639. URL <https://www.ajnr.org/content/41/8/1538>.

601 Andre Kassis, Urs Hengartner, and Yaoliang Yu. Unlocking the potential of adaptive attacks on
 602 diffusion-based purification. *arXiv preprint arXiv:2411.16598*, 2024.

603

604 Jeewon Kim, Wonil Lee, Beomgu Kang, Seohee So, and HyunWook Park. A noise robust image
 605 reconstruction deep neural network with cycle interpolation. In *Proc. ISMRM*, pp. 3717, 2023.

606 Florian Knoll, Kerstin Hammernik, Erich Kobler, Thomas Pock, Michael P Recht, and Daniel K
 607 Sodickson. Assessment of the generalization of learned image reconstruction and the potential
 608 for transfer learning. *Magn Reson Med*, 81(1):116–128, 2019.

609

610 Florian Knoll, Kerstin Hammernik, Chi Zhang, Steen Moeller, Thomas Pock, Daniel K Sodickson,
 611 and Mehmet Akçakaya. Deep-learning methods for parallel magnetic resonance imaging recon-
 612 struction: A survey of the current approaches, trends, and issues. *IEEE Sig Proc Mag*, 37(1):
 613 128–140, January 2020a.

614

615 Florian Knoll, Jure Zbontar, Anuroop Sriram, Matthew J Muckley, Mary Bruno, Aaron Defazio,
 616 Marc Parente, Krzysztof J Geras, Joe Katsnelson, Hersh Chandarana, et al. fastmri: A publicly
 617 available raw k-space and dicom dataset of knee images for accelerated MR image reconstruction
 618 using machine learning. *Radiology: Artificial Intelligence*, 2(1):e190007, 2020b.

619

620 Shijun Liang, Van Hoang Minh Nguyen, Jinghan Jia, Ismail Alkhouri, Sijia Liu, and Saiprasad
 621 Ravishankar. Robust MRI reconstruction by smoothed unrolling (SMUG). *arXiv:2312.07784*,
 622 2023.

623

624 Pengju Liu, Hongzhi Zhang, Wei Lian, and Wangmeng Zuo. Multi-level wavelet convolutional
 625 neural networks. *IEEE Access*, 7:74973–74985, 2019.

626

627 Kai Lønning, Patrick Putzky, Jan-Jakob Sonke, Liesbeth Reneman, Matthan WA Caan, and Max
 628 Welling. Recurrent inference machines for reconstructing heterogeneous MRI data. *Medical
 629 Image Analysis*, 53:64–78, 2019.

630

631 Michael Lustig and John M Pauly. Spirit: iterative self-consistent parallel imaging reconstruction
 632 from arbitrary k-space. *Magn Reson Med*, 64(2):457–471, 2010.

633

634 Michael Lustig, David Donoho, and John M Pauly. Sparse MRI: The application of compressed
 635 sensing for rapid MR imaging. *Magn Reson Med.*, 58(6):1182–1195, December 2007.

636

637 Aleksander Mkadry, Aleksandar Makelov, Ludwig Schmidt, Dimitris Tsipras, and Adrian Vladu.
 638 Towards deep learning models resistant to adversarial attacks. *ICLR*, 2018.

639

640 Vishal Monga, Yuelong Li, and Yonina C Eldar. Algorithm unrolling: Interpretable, efficient deep
 641 learning for signal and image processing. *IEEE Sig Proc Mag*, 38(2):18–44, 2021.

642

643 Seyed-Mohsen Moosavi-Dezfooli, Alhussein Fawzi, and Pascal Frossard. Deepfool: a simple and
 644 accurate method to fool deep neural networks. In *Proc CVPR*, pp. 2574–2582, 2016.

645

646 Matthew J Muckley, Bruno Riemenschneider, Alireza Radmanesh, Sunwoo Kim, Geunu Jeong,
 647 Jingyu Ko, Yohan Jun, Hyungseob Shin, Dosik Hwang, Mahmoud Mostapha, et al. Results of the
 648 2020 fastMRI challenge for machine learning MR image reconstruction. *IEEE Transactions on
 649 Medical Imaging*, 40(9):2306–2317, 2021.

650

651 Weili Nie, Brandon Guo, Yujia Huang, Chaowei Xiao, Arash Vahdat, and Anima Anandkumar.
 652 Diffusion models for adversarial purification. *arXiv preprint arXiv:2205.07460*, 2022.

653

654 Aaditya Prakash, Nick Moran, Solomon Garber, Antonella DiLillo, and James Storer. Deflecting
 655 adversarial attacks with pixel deflection. In *Proc CVPR*, pp. 8571–8580, 2018.

648 Aniket Pramanik, M Bridget Zimmerman, and Mathews Jacob. Memory-efficient model-based deep
 649 learning with convergence and robustness guarantees. *IEEE transactions on computational imaging*, 9:260–275, 2023.
 650

651 Klaas P. Pruessmann, Markus Weiger, Markus B. Scheidegger, and Peter Boesiger. SENSE: Sensitivity
 652 encoding for fast MRI. *Magn Reson Med*, 42(5):952–962, Nov 1999.
 653

654 Han Qiu, Yi Zeng, Qinkai Zheng, Tianwei Zhang, Meikang Qiu, and Gerard Memmi. Mitigating
 655 advanced adversarial attacks with more advanced gradient obfuscation techniques. *arXiv preprint*
 656 *arXiv:2005.13712*, 2020.
 657

658 Ankit Raj, Yoram Bresler, and Bo Li. Improving robustness of deep-learning-based image recon-
 659 struction. In *International Conference on Machine Learning*, pp. 7932–7942. PMLR, 2020.
 660

661 Zaccharie Ramzi, Philippe Ciuciu, and Jean-Luc Starck. XPDNet for MRI reconstruction: An
 662 application to the 2020 fastMRI challenge. *arXiv:2010.07290*, 2020.
 663

664 Aref Rekavandi, Farhad Farokhi, Olga Ohrimenko, and Benjamin Rubinstein. Certified adversarial
 665 robustness via randomized α -smoothing for regression models. *Advances in Neural Information*
 666 *Processing Systems*, 37:134127–134150, 2024.
 667

668 Hadi Salman, Mingjie Sun, Greg Yang, Ashish Kapoor, and J Zico Kolter. Denoised smoothing: A
 669 provable defense for pretrained classifiers. *Proc NeurIPS*, 33:21945–21957, 2020.
 670

671 Burhan Ul Haque Sheikh and Aasim Zafar. Removing adversarial noise in x-ray images via total
 672 variation minimization and patch-based regularization for robust deep learning-based diagnosis.
 673 *Journal of Imaging Informatics in Medicine*, 37(6):3282–3303, 2024.
 674

675 Anuroop Sriram, Jure Zbontar, Tullie Murrell, Aaron Defazio, C Lawrence Zitnick, Nafissa
 676 Yakubova, Florian Knoll, and Patricia Johnson. End-to-end variational networks for accelerated
 677 MRI reconstruction. In *MICCAI*, pp. 64–73. Springer, 2020.
 678

679 Alfred Stadler, Wolfgang Schima, Ahmed Ba-Ssalamah, Joachim Kettenbach, and Edith Eisenhuber.
 680 Artifacts in body MR imaging: their appearance and how to eliminate them. *European radiology*,
 681 17(5):1242–1255, 2007.
 682

683 Julián Tachella, Dongdong Chen, and Mike Davies. Unsupervised learning from incomplete mea-
 684 surements for inverse problems. *Proc NeurIPS*, pp. 4983–4995, 2022.
 685

686 Radu Timofte, Eirikur Agustsson, Luc Van Gool, Ming-Hsuan Yang, and Lei Zhang. Ntire 2017
 687 challenge on single image super-resolution: Methods and results. In *Proc CVPR Workshops*, pp.
 688 114–125, 2017.
 689

690 Florian Tramer, Nicholas Carlini, Wieland Brendel, and Aleksander Madry. On adaptive attacks to
 691 adversarial example defenses. *Proc NeurIPS*, 33:1633–1645, 2020.
 692

693 Dimitris Tsipras, Shibani Santurkar, Logan Engstrom, Alexander Turner, and Aleksander Madry.
 694 Robustness may be at odds with accuracy. *ICLR*, 2019.
 695

696 Martin Uecker, Peng Lai, Mark J Murphy, Patrick Virtue, Michael Elad, John M Pauly, Shreyas S
 697 Vasanawala, and Michael Lustig. ESPIRiT—an eigenvalue approach to autocalibrating parallel
 698 MRI: where SENSE meets GRAPPA. *Magn Reson Med*, 71(3):990–1001, 2014.
 699

700 Lukas Winter, João Periquito, Christoph Kolbitsch, Ruben Pellicer-Guridi, Rita G Nunes, Martin
 701 Häuer, Lionel Broche, and Tom O'Reilly. Open-source magnetic resonance imaging: improving
 702 access, science, and education through global collaboration. *NMR in Biomedicine*, 37(7):e5052,
 703 2024.
 704

705 Cihang Xie, Jianyu Wang, Zhishuai Zhang, Zhou Ren, and Alan Yuille. Mitigating adversarial
 706 effects through randomization. *arXiv preprint arXiv:1711.01991*, 2017.
 707

708 Burhaneddin Yaman, Seyed A. H. Hosseini, Steen Moeller, Jutta Ellermann, Kâmil Uğurbil, and
 709 Mehmet Akçakaya. Self-supervised learning of physics-guided reconstruction neural networks
 710 without fully sampled reference data. *Magn Reson Med.*, 84(6):3172–3191, December 2020.

702 Burhaneddin Yaman, Hongyi Gu, Seyed Amir Hosseini, Omer Burak Demirel, Steen
 703 Moeller, Jutta Ellermann, Kâmil Uğurbil, and Mehmet Akçakaya. Multi-mask self-supervised
 704 learning for physics-guided neural networks in highly accelerated magnetic resonance imaging.
 705 *NMR in Biomedicine*, 35(12):e4798, 2022a.

706 Burhaneddin Yaman, Seyed Amir Hosseini, and Mehmet Akçakaya. Zero-shot self-
 707 supervised learning for MRI reconstruction. In *ICLR*, 2022b. URL <https://openreview.net/forum?id=085y6YPaYjP>.

708

710 Zonghan Yang, Tianyu Pang, and Yang Liu. A closer look at the adversarial robustness of deep
 711 equilibrium models. *Proc NeurIPS*, 35:10448–10461, 2022.

712 George Yiasemis, Nikita Moriakov, Dimitrios Karkalousos, Matthan Caan, and Jonas Teuwen. DI-
 713 RECT: deep image REConstruction toolkit. *Journal of Open Source Software*, 7(73):4278, 2022a.
 714 doi: 10.21105/joss.04278. URL <https://doi.org/10.21105/joss.04278>.

715

716 George Yiasemis, Jan-Jakob Sonke, Clarisa Sánchez, and Jonas Teuwen. Recurrent variational
 717 network: a deep learning inverse problem solver applied to the task of accelerated MRI recon-
 718 struction. In *Proc CVPR*, pp. 732–741, 2022b.

719 Maxim Zaitsev, Julian Maclare, and Michael Herbst. Motion artifacts in MRI: A complex problem
 720 with many partial solutions. *Journal of Magnetic Resonance Imaging*, 42(4):887–901, 2015.

721

722 Chi Zhang and Mehmet Akçakaya. Uncertainty-guided physics-driven deep learning reconstruction
 723 via cyclic measurement consistency. In *2024 IEEE ICASSP*, pp. 13441–13445, 2024. doi: 10.
 724 1109/ICASSP48485.2024.10447594.

725

726 Chi Zhang, Jinghan Jia, Burhaneddin Yaman, Steen Moeller, Sijia Liu, Mingyi Hong, and Mehmet
 727 Akçakaya. Instabilities in conventional multi-coil MRI reconstruction with small adversarial per-
 728 turbations. In *2021 55th Asilomar Conference on Signals, Systems, and Computers*, pp. 895–899.
 729 IEEE, 2021.

730

731 Chi Zhang, Omer Burak Demirel, and Mehmet Akçakaya. Cycle-consistent self-supervised learning
 732 for improved highly-accelerated MRI reconstruction. In *2024 IEEE ISBI*, pp. 1–5. IEEE, 2024.

733

734 Tiejun Zhao and Xiaoping Hu. Iterative GRAPPA (iGRAPPA) for improved parallel imaging re-
 735 construction. *Magn Reson Med*, 59(4):903–907, Apr 2008.

736

737 Zongwei Zhou, Md Mahfuzur Rahman Siddiquee, Nima Tajbakhsh, and Jianming Liang. Unet++:
 738 A nested u-net architecture for medical image segmentation. In *Deep Learning in Medical Image
 739 Analysis and Multimodal Learning for Clinical Decision Support*, pp. 3–11. Springer, 2018.

740

741

742

743

744

745

746

747

748

749

750

751

752

753

754

755

756 A IMPLEMENTATION DETAILS
757758 A.1 PD-DL NETWORK DETAILS
759

760 **MoDL** implementation is based on (Aggarwal et al., 2019), unrolling variable splitting with
761 quadratic penalty algorithm (Fessler, 2020) for 10 steps. The proximal operator for the regularizer
762 is implemented with a ResNet (Yaman et al., 2020; Hosseini et al., 2020; Demirel et al., 2023b), and
763 data fidelity term is implemented using conjugate gradient, itself unrolled for 10 iterations (Aggar-
764 wal et al., 2019). The ResNet comprises input and output convolutional layers, along with 15 resi-
765 dual blocks. Each residual block has a skip connection and two convolutional blocks with a rectified
766 linear unit in between. At the end of each residual block, there is a constant scaling layer (Timofte
767 et al., 2017), and the weights are shared among different blocks (Aggarwal et al., 2019).

768 **XPDNet** implementation is based on (Yiasemis et al., 2022a) and follows (Ramzi et al., 2020),
769 which unrolls the primal dual hybrid gradient (PDHG) algorithm (Chambolle & Pock, 2011) for 10
770 steps. Each step contains k-space and image correction in sequence, where form the data fidelity and
771 regularizer respectively. XPDNet applies the undersampling mask on the subtraction of the interme-
772 diate k-space with original measurements in k-space correction step. Image correction/regularizer
773 is implemented using multi-scale wavelet CNN (MWCNN) (Liu et al., 2019) followed by a convolu-
774 tional layer. Inspired by PDNet (Adler & Öktem, 2018), it uses a modified version of PDHG
775 to utilize a number of optimization parameters instead of just using the previous block’s output. 5
776 primal and 1 dual variables are used during the unrolling process, and the weights are not shared
777 across the blocks.

778 **RIM** implementation based on (Yiasemis et al., 2022a) as described in (Lønning et al., 2019) unrolls
779 the objective for 16 time steps, where each utilizes a recurrent time step. Each time step takes the
780 previous reconstruction, hidden states and the gradient of negative log-likelihood (as data fidelity
781 term) and outputs the incremental step in image domain to take using a gated recurrent units (GRU)
782 structure (Cho, 2014), where it utilizes depth 1 and 128 hidden channels. Parameters are shared
783 across different recurrent blocks.

784 **E2E-VarNet** uses the publicly available implementation (Sriram et al., 2020), and like variational
785 networks, implements an unrolled network to solve the regularized least squares objective using
786 gradient descent. The algorithm is unrolled for 12 steps. Each step combines data fidelity with
787 a regularizer. Data fidelity term applies the undersampling mask after subtraction of intermediate
788 k-space from the measurements, while learned regularizer is implemented via U-Net (Zhou et al.,
789 2018), where it uses 4 number of pull layers and 18 number of output channels after first convolution
790 layer. Weights are not shared across blocks.

791 **Recurrent VarNet** uses the publicly available implementation (Yiasemis et al., 2022b) estimates a
792 least squares variational problem by unrolling with gradient descent for 8 steps. Each iteration is
793 a variational block, comprising data fidelity and regularizer terms. Data fidelity term calculates the
794 difference between current level k-space and the measurements on undersampling locations, where
795 regularizer utilizes gated recurrent units (GRU) structure (Cakir et al., 2017). Each unroll block uses
796 4 of these GRUs with 128 number of hidden channels for regularizer. Parameters are not shared
797 across different blocks (Yiasemis et al., 2022b).

798 As described in the main text, all methods were retrained on the respective datasets with supervised
799 learning for maximal performance. Unsupervised training that only use undersampled data (Ya-
800 man et al., 2020; 2022a; Akçakaya et al., 2022) can also be used, though this typically does not
801 outperform supervised learning.

802 A.2 COMPARISON METHODS AND ALGORITHMIC DETAILS
803

804 **SMUG** (Liang et al., 2023) trains the same PD-DL network we used for MoDL using smoothing
805 via Eq. (6). Smoothing is implemented using 10 Monte-Carlo samples (Liang et al., 2023), with a
806 noise level of 0.01, where data is normalized in image domain.

807 **Adversarial Training (AT)** method also uses the same network structure as MoDL. Here, each
808 adversarial sample is generated with 10 iterations of PGD (Mkadry et al., 2018) with $\epsilon = 0.01$ and
809 $\alpha = \epsilon/5$. Data are normalized to $[0, 1]$ in image domain.

810 B HERRINGBONE ARTIFACT DETAILS
811

812 Herringbone artifacts can arise from several factors, including electromagnetic spikes by gradient
813 coils, fluctuating in power supply, and RF pulse dependencies (Stadler et al., 2007). These factors
814 introduce impulse-like spikes in the k-space, and if their intensities are high enough, they mani-
815 fest as herringbone-like artifacts across the entire image, even for fully-sampled acquisitions (Jin
816 et al., 2017). Here, we hypothesized that DL-based reconstruction of undersampled datasets may
817 be affected by such spikes even if the intensities are not visibly apparent in the zero-filled images
818 or in fully-sampled datasets. The standard spike modeling for herringbone artifacts uses a sum of
819 impulses, as follows:

$$820 \quad \tilde{\mathbf{y}}_{\Omega} = \mathbf{y}_{\Omega} + \sum_{j=1}^D \xi_j \delta_{i_j}, \quad (12)$$

821 where δ_{i_j} is a delta/impulse on the i_j^{th} index (i.e. the canonical basis vector \mathbf{e}_{i_j}), ξ_j is the strength
822 of the spike on the i_j^{th} index, and D is the number of spikes. Thus, we use the same model and use
823 a sparse and bounded adversarial attack for DL-based reconstructions. In particular, we randomly
824 select the locations of $\{i_j\}_{j=1}^D$ with heavier sampling in low-frequencies to highlight the traditional
825 herringbone-type artifacts visibly. While selecting the high-frequency locations is also feasible, the
826 resulting artifacts appear less sinusoidal. Let $\mathbf{w}_{\text{hb}} = \sum_{j=1}^D \xi_j \delta_{i_j}$ with unknown spike strength ξ_j ,
827 we optimize:

$$828 \quad \arg \max_{\mathbf{w}_{\text{hb}}: \|\mathbf{w}_{\text{hb}}\|_{\infty} \leq \epsilon} \mathcal{L}(f(\mathbf{E}_{\Omega}^H(\mathbf{y}_{\Omega} + \mathbf{w}_{\text{hb}}), \mathbf{E}_{\Omega}; \theta), f(\mathbf{E}_{\Omega}^H \mathbf{y}_{\Omega}, \mathbf{E}_{\Omega}; \theta)). \quad (13)$$

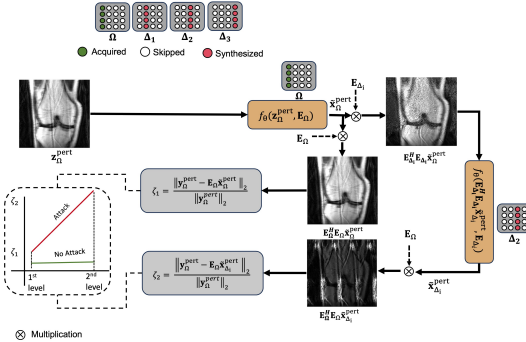
830 This was solved using PGD (Mkadry et al., 2018) with 10 iterations, $D = 25$, and $\epsilon = 0.06 \cdot \max(\mathbf{y}_{\Omega})$,
831 ensuring that the resulting zero-filled image remained visibly identical to the clean zero-filled image.

832 C ATTACK DETECTION USING SIMULATED K-SPACE
833

834 The description of the attack propagation suggests a methodology for detecting these attacks. Noting
835 that the process is best understood in terms of consistency with acquired data in k-space, we perform
836 detection in k-space instead of attempting to understand the differences between subsequent recon-
837 struction in image domain, which is not clearly characterized. In particular, we define two stages of
838 k-space errors in terms of \mathbf{y}_{Ω} for $\tilde{\mathbf{x}}_{\Omega}$ and $\tilde{\mathbf{x}}_{\Delta_i}$, which were defined in Eq. (7)-Eq. (8) as follows:

$$839 \quad \zeta_1 = \frac{\|\mathbf{y}_{\Omega} - \mathbf{E}_{\Omega} \tilde{\mathbf{x}}_{\Omega}\|_2}{\|\mathbf{y}_{\Omega}\|_2}, \quad \zeta_2 = \frac{\|\mathbf{y}_{\Omega} - \mathbf{E}_{\Omega} \tilde{\mathbf{x}}_{\Delta_i}\|_2}{\|\mathbf{y}_{\Omega}\|_2}. \quad (14)$$

840 From the previous description ζ_1 is expected to be small with or without attack. However, ζ_2
841 is expected to be much larger under the attack, while it should be almost at the same level as
842 ζ_1 without an attack. Thus, we check the difference between these two normalized errors,
843 $\zeta_2 - \zeta_1$, and detect an attack if it is greater than a dataset-dependent threshold. The process is
844 depicted in Fig. 6, and summarized in Algorithm 2. Fig. 7 shows how $\zeta_2 - \zeta_1$ changes for knee and brain datasets for both PGD and
845 FGSM attacks on normalized zero-filled images for $\epsilon \in \{0.01, 0.02\}$. It is clear that cases with
846 an attack vs. non-perturbed inputs are separated by a dataset-dependent threshold. Note that given the sensitivity of PD-DL networks to
847 SNR and acceleration rate changes, this dataset
848 dependence is not surprising (Knoll et al., 2019), and can be evaluated offline for a given trained
849 model.



850 Figure 6: Propagation of the attack in Fig. 1a motivates tracking the normalized ℓ_2 error on sam-
851 pled k-space locations after reconstruction; a large
852 change in this error indicates an attack.

864 D QUANTITATIVE RESULTS AND REPRESENTATIVE EXAMPLES 865

866 Due to space constraints, the figures
867 and results in the main text focused
868 on ℓ_∞ attacks generated with unsu-
869 pervised PGD (Mkadry et al., 2018),
870 as mentioned in Section 4.1. This
871 section provides the corresponding
872 results on related attack types men-
873 tioned in Section 4.2.

874 D.1 HIGHER 875 ATTACK STRENGTHS 876

877 Tab. 3 summarizes the quantitative
878 population metrics for different at-
879 tack strengths, ϵ , complementing the
880 representative examples shown in
881 Fig. 3 of Section 3.2. These quan-
882 titative results align with the visual ob-
883 servations.

884 D.2 QUANTITATIVE METRICS 885 FOR DIFFERENT NETWORKS 886

887 Tab. 4 shows that the quantitative
888 metrics for the proposed attack mi-
889 tigation strategy improve substan-
890 tially compared to the attack for all un-
891 rolled networks, aligning with the ob-
892 servations in Fig. 4.

893 D.3 DIFFERENT ADVERSARIAL 894 TRAINING METHODS 895

896 This subsection provides an alter-
897 native implementation of the adver-
898 sarial training based on Eq. (5) with $\lambda =$
899 1 to balance the perturbed and clean
900 input, instead of Eq. (4) that was pro-
901 vided in the main text as a compari-
902 son. Results in Tab. 5 show
903 that the version in the main text outper-
904 forms the alternative version provided here.

905 D.4 MITIGATION PERFORMANCE ON NON-PERTURBED DATA 906

907 Hence, the mitigation does not degrad-
908 e the quality of the clean inputs, and does not in-
909 cur large computational costs, as it effec-
910 tively converges in a single iteration. Vi-
911 sual examples of this process are depicted
912 in Fig. 8. As discussed in Section 3.1,
913 Algorithm 1 does not compromise the re-
914 construction quality if the input is un-
915 perturbed. This is because, with an unper-
916 turbed input image in Eq. (10), the intermediate recon-
917 struction remains consistent with the mea-
918 surements. As a result, the objective value
919 remains close to zero and stays near that level until the end, indicating the mitiga-
920 tion starts from an almost optimal point of
921 the objective function.

922 D.5 SUPERVISED ATTACKS 923

Algorithm 2 Attack Detection

Require: $\mathbf{z}_\Omega, \mathbf{E}_\Omega, \mathbf{E}_\Delta, f(\cdot, \cdot; \theta), \tau \triangleright$ Input parameters
Ensure: **True** or **False**, presence of attack \triangleright Output

- 1: $\tilde{\mathbf{x}}_\Omega \leftarrow f(\mathbf{z}_\Omega, \mathbf{E}_\Omega; \theta)$
- 2: $\mathbf{y}_\Delta \leftarrow \mathbf{E}_\Delta \tilde{\mathbf{x}}_\Omega + \tilde{\mathbf{n}}$
- 3: $\tilde{\mathbf{x}}_\Delta \leftarrow f(\mathbf{E}_\Delta^H \mathbf{y}_\Delta, \mathbf{E}_\Delta; \theta)$
- 4: $\zeta_1 = \frac{\|\mathbf{y}_\Omega - \mathbf{E}_\Omega \tilde{\mathbf{x}}_\Omega\|_2}{\|\mathbf{y}_\Omega\|_2}$
- 5: $\zeta_2 = \frac{\|\mathbf{y}_\Omega - \mathbf{E}_\Omega \tilde{\mathbf{x}}_\Delta\|_2}{\|\mathbf{y}_\Omega\|_2}$
- 6: If $\zeta_2 - \zeta_1 \geq \tau$ **True**, else **False**

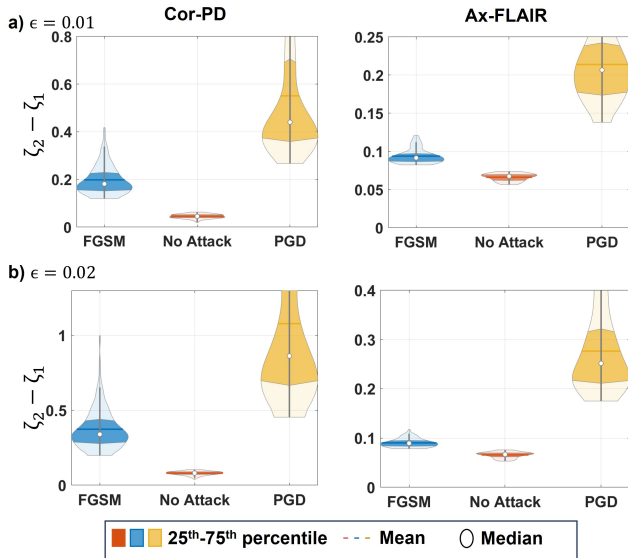


Figure 7: Attack detection for different datasets. $\zeta_2 - \zeta_1$ for different attack types are clearly separated from the no attack case. For stronger attack, $\epsilon = 0.02$, $\zeta_2 - \zeta_1$ is more easily distinguishable. The violin plots show the median and [25, 75] percentile in darker colors for easier visualization. Results in Tab. 5 show that the version in the main text outperforms the alternative version provided here.

Table 3: Different attack strengths: Quantitative met-
rics on all test slices of Cor-PD.

ϵ	Metric	SMUG	Adversarial Training (AT)	Proposed Method + MoDL / SMUG / AT
0.01	PSNR	28.22	33.99	35.14/34.85/ 36.57
	SSIM	0.79	0.92	0.92/0.92/ 0.94
0.02	PSNR	21.86	30.91	33.25/32.97/ 33.42
	SSIM	0.61	0.88	0.91/0.91/ 0.93

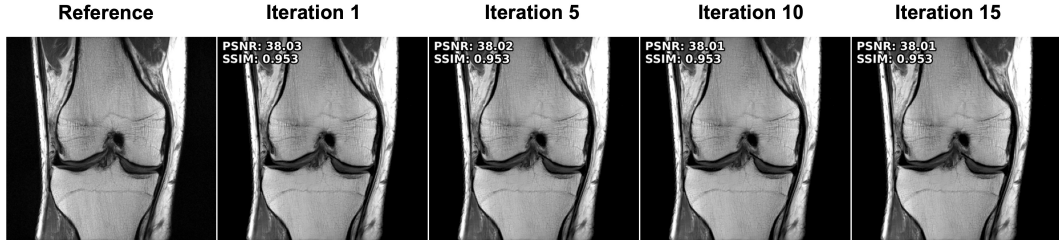


Figure 8: Performance of mitigation algorithm on non-perturbed data. The mitigation effectively converges in one iteration. As shown, the algorithm maintains the quality of the clean input.

While Section 4.1 and 4.2 focused on unsupervised attacks due to practicality, here we provide additional experiments with supervised attacks, even though they are not realistic for MRI reconstruction systems. Tab. 6 shows that the proposed method is equally efficient in mitigating supervised attacks.

D.6 FGSM ATTACK

In Section 4.1, we used the PGD method for attack generation due to the more severe nature of the attacks. Here, we provide additional experiments with FGSM attacks (Goodfellow et al., 2015).

Tab. 7 show results using SMUG, adversarial training and our method with FGSM attacks with $\epsilon = 0.01$. Corresponding visual examples are depicted in Fig. 9, showing that all methods perform better under FGSM compared to PGD attacks.

D.7 ℓ_2 ATTACKS IN K-SPACE

ℓ_2 attacks have been used in k-space due to the large variation in intensities in the Fourier domain (Raj et al., 2020). To complement the ℓ_∞ attacks in image domain that was provided in the main text, here we provide results for ℓ_2 attacks in k-space, generated using PGD (Mkadry et al., 2018) for 5 iterations, with $\epsilon = 0.05 \cdot \|\mathbf{y}_\Omega\|_2$ and $\alpha = \frac{\epsilon}{5}$. Fig. 10 depicts representative re-

Table 4: Quantitative metrics for different unrolled networks.

Network	Metric	With Attack	After Proposed Mitigation
XPDNet	PSNR	25.49	29.43
	SSIM	0.67	0.80
RIM	PSNR	19.63	34.81
	SSIM	0.39	0.90
E2E-VarNet	PSNR	24.24	29.52
	SSIM	0.59	0.84
Recurrent VarNet	PSNR	22.27	29.24
	SSIM	0.52	0.84

Table 5: Comparison of adversarial training approaches.

Method	Metric	With Attack
AT with Eq. (4)	PSNR	33.99
	SSIM	0.92
AT with Eq. (5)	PSNR	33.61
	SSIM	0.91
AT with Eq. (4) + Proposed Method	PSNR	36.17
	SSIM	0.94
AT with Eq. (5) + Proposed Method	PSNR	36.91
	SSIM	0.94

Table 6: Mitigation with supervised vs. unsupervised attacks.

Attack Method	Metric	Proposed Method
Unsupervised Attack	PSNR	32.44
	SSIM	0.91
Supervised Attack	PSNR	32.55
	SSIM	0.91

Table 7: FGSM attack: Quantitative metrics on all test slices of Ax-FLAIR.

Metric	SMUG	Adversarial Training (AT)	Proposed Method + MoDL / SMUG / AT
PSNR	36.24	35.61	36.24 / 35.13 / 36.06
SSIM	0.93	0.93	0.93 / 0.92 / 0.93

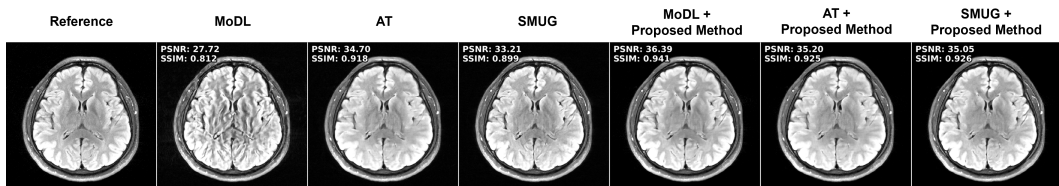


Figure 9: Performance of different methods under FGSM attack.

972 constructions with ℓ_2 attacks in k-space using baseline MoDL, adversarial training and our
 973 proposed mitigation. Tab. 8 shows comparison of adversarial training and the proposed
 974 method on Cor-PD datasets, highlighting the efficacy of our method in this setup as well.
 975 We also emphasize that the ℓ_∞ image domain attacks are easily converted to attacks in k-
 976 space, which are non-zero only on indices specified by Ω , as described in Section 2.2.
 977

978 D.8 NON-UNIFORM UNDERSAMPLING PATTERNS

980 While the main text focused on uniform undersampling, which is considered to be a harder
 981 problem (Hammerink et al., 2018; Yaman et al., 2020), here we describe results with random
 982 undersampling, generated with a variable density Gaussian pattern (Aggarwal et al., 2019).
 983

984 All networks were retrained for such undersampling patterns. The attack generation and our
 985 mitigation algorithms were applied without any
 986 changes, as described in the main text. Fig. 11
 987 shows representative examples for different methods, highlighting that our method readily extends
 988 to non-uniform undersampling patterns. Tab. 9
 989 summarizes the quantitative metrics for this case,
 990 showing that the proposed mitigation improves upon MoDL or adversarial training alone.
 991

992 E BLIND MITIGATION

993 This section shows that in addition to not needing
 994 any retraining for mitigation, our approach
 995 does not require precise information about how
 996 the attack is generated. Fig. 12 shows how
 997 the reconstruction improves as we use linear
 998 schedulers to find the optimum (ϵ, α) values.
 999 Top row shows the tuning of ϵ while we keep
 1000 the step size α constant. After the cyclic loss in Eq. (10)
 1001 stops decreasing, we fix this $\tilde{\epsilon}$ for
 1002 the projection ball. The bottom row shows the effect of decreasing α for this $\tilde{\epsilon}$ value, from
 1003 right to left. For this purpose, our linear scheduler for ϵ starts from 0.04 and decreases by
 1004 0.01 each step until the cyclic loss stabilizes. Then, step size α starts from a large value of
 1005 ϵ and gradually decreases, ending at $\epsilon/3.5$ until the cyclic loss shows no further improvement.
 1006

1007 As mentioned in the main text, since the ℓ_∞ ball
 1008 contains the ℓ_2 ball of the same radius, and noting
 1009 the unitary nature of the Fourier transform
 1010 in regards to ℓ_2 attack strengths in k-space
 1011 versus image domain, we always use the ℓ_∞ ball
 1012 for blind mitigation. Furthermore, we provide
 1013 results for using blind mitigation with ℓ_2 attacks in k-space.
 1014



Figure 10: Representative reconstructions under ℓ_2 attack on measurements with $\epsilon = 0.05 \cdot \|\mathbf{y}_\Omega\|_2$ using MoDL, adversarial training, and our proposed method.

995

Table 8: Mitigation results for ℓ_2 attacks in k-space.

Method	Metric	ℓ_2 Attack
Adversarial Training	PSNR	33.37
	SSIM	0.88
Proposed Method + MoDL	PSNR	34.21
	SSIM	0.89

Table 9: Attacks on non-uniform undersampling.

Metric	MoDL	Adversarial Training (AT)	Proposed Method + MoDL / AT
PSNR	22.30	32.22	31.82 / 34.12
SSIM	0.62	0.89	0.87 / 0.92

Figure 11: Representative reconstructions for non-uniform undersampling reconstructions using MoDL, adversarial training, and our proposed method under adversarial attacks.

1026
 1027 Fig. 13 depicts example reconstructions with ℓ_2
 1028 attacks in k-space using baseline MoDL and our
 1029 blind mitigation approach. Tab. 10 compares
 1030 our blind mitigation approach to our miti-
 1031 gation strategy with known attack type and
 1032 level, showing that blind mitigation performs
 1033 on-par with the latter for both ℓ_2 attacks in k-
 1034 space and ℓ_∞ attacks in image domain.

F FURTHER DETAILS ON ADAPTIVE ATTACKS

This section contains more information about adaptive attack generation and visual examples. As discussed earlier, strong performance against iterative optimization-based attacks is not necessarily a good indicator of robustness and must be evaluated under adaptive attacks (Qiu et al., 2020; Guo et al., 2017; Prakash et al., 2018; Xie et al., 2017; Buckman et al., 2018). As mentioned in the main text, to generate the adaptive attack we unroll Algorithm 1 for T iterations. The memory requirements of larger T was handled by checkpointing (Chen et al., 2023; Kassis et al., 2024). Furthermore, the presence of $\tilde{\mathbf{n}}$ in Eq. (10) may suggest stochasticity in the system (Kassis et al., 2024). However, $\tilde{\mathbf{n}}$ is pre-calculated for a given input in our mitigation algorithm, and held constant throughout the mitigation. To make the adaptive attack as strong as possible, we pass this information about $\tilde{\mathbf{n}}$ to the adaptive attack as well, thus letting it have oracle knowledge about it. Finally, for maximal performance of the attack, we first tuned λ in Eq. (11) empirically, then generated the adaptive attacks for $T \in \{10, 25, 50, 100\}$. Details on tuning of λ and verification of gradient obfuscation avoidance in our adaptive attacks are detailed below.

F.1 HYPERPARAMETER TUNING FOR ADAPTIVE ATTACKS

The parameter λ in eq. (11) balances the two terms involved in the adaptive attack generation. A higher λ produces a perturbation with more focus on bypassing the defense strategy, while potentially not generating a strong enough attack for the baseline. Conversely, a small λ may not lead to sufficient adaptivity in the attack generation. To this end, we computed the population-average PSNRs of the reconstruction after the iterative mitigation algorithm on a subset of Cor-PD for various λ values for $T \in \{10, 25\}$, as shown in Tab. 11.

These results show that $\lambda = 5$ leads to the most destructive attack against our mitigation algorithm, and was subsequently used for adaptive attack generation in Section 4.2.

F.2 VERIFICATION OF GRADIENT OBFUSCATION AVOIDANCE

While our adaptive attack implements the exact gradient to avoid gradient obfuscation (including shattered, stochastic, and vanishing gradients (Athalye et al., 2018)), there are some methods to verify that gradients are indeed not obfuscated (Athalye et al., 2018). In particular, we tested two well-established key criteria: 1) One-step attacks should not outperform iterative-based ones, and 2) Increasing the perturbation bound (i.e. ϵ) should lead to a greater disruption. Tab. 12 summarizes these two criteria, showing PSNRs of the iterative mitigation algorithm

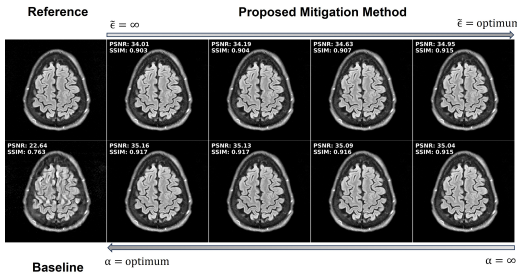


Figure 12: Blind mitigation process of finding the optimum (ϵ, α) parameters and corresponding results. Top row shows ϵ optimization for a fixed α , while the bottom row shows α optimization for the optimum ϵ . This joint optimization leads to a 1.15dB gain over the initial estimate.

This section contains more information about adaptive attack generation and visual examples. As discussed earlier, strong performance against iterative optimization-based attacks is not necessarily a good indicator of robustness and must be evaluated under adaptive attacks (Qiu et al., 2020; Guo et al., 2017; Prakash et al., 2018; Xie et al., 2017; Buckman et al., 2018). As mentioned in the main text, to generate the adaptive attack we unroll Algorithm 1 for T iterations. The memory requirements of larger T was handled by checkpointing (Chen et al., 2023; Kassis et al., 2024). Furthermore, the presence of $\tilde{\mathbf{n}}$ in Eq. (10) may suggest stochasticity in the system (Kassis et al., 2024). However, $\tilde{\mathbf{n}}$ is pre-calculated for a given input in our mitigation algorithm, and held constant throughout the mitigation. To make the adaptive attack as strong as possible, we pass this information about $\tilde{\mathbf{n}}$ to the adaptive attack as well, thus letting it have oracle knowledge about it. Finally, for maximal performance of the attack, we first tuned λ in Eq. (11) empirically, then generated the adaptive attacks for $T \in \{10, 25, 50, 100\}$. Details on tuning of λ and verification of gradient obfuscation avoidance in our adaptive attacks are detailed below.

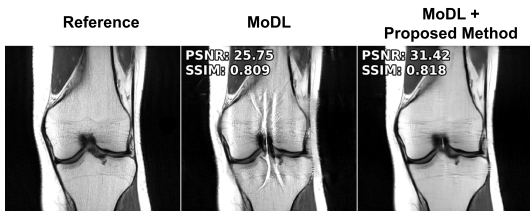


Figure 13: Representative reconstructions under ℓ_2 attack using MoDL and our proposed blind mitigation.

Table 10: Blind mitigation for ℓ_2 (k-space, $\epsilon = 0.05 \cdot \|\mathbf{y}_\Omega\|_2$) and ℓ_∞ (image domain, $\epsilon = 0.01$) attacks on Cor-PD.

Attack Method	Metric	Proposed Method (ℓ_∞ attack)	Proposed Method (ℓ_2 attack)
Knowing the Attack	PSNR	35.14	34.21
	SSIM	0.92	0.89
Blind Mitigation	PSNR	34.72	33.73
	SSIM	0.92	0.88

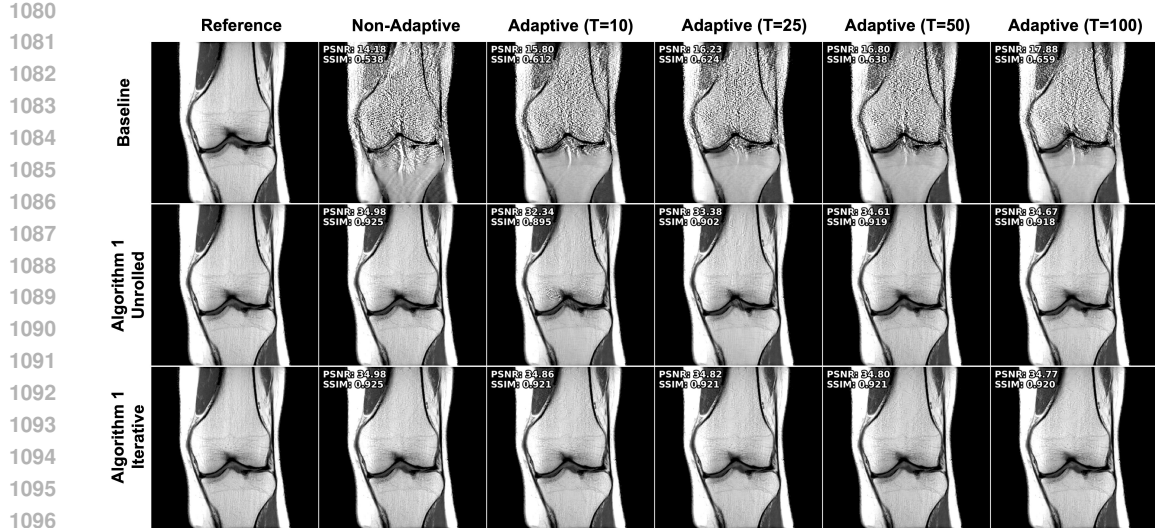


Figure 14: Representative examples of the mitigation algorithm outputs for adaptive attacks. The number of unrolls $T \in \{10, 25, 50, 100\}$ specified for each adaptive attack on the top. The top row is the baseline reconstruction, where the non-adaptive attack shows more artifacts than adaptive ones, as expected. The second row shows the mitigation outputs using the unrolled version of Algorithm 1, where the number of unrolls are matched between the adaptive attack generation and mitigation. At smaller T values, the unrolled mitigation suffers from performance degradation. Finally, the last row shows the results of the iterative mitigation algorithm on the adaptive attacks. Iterative mitigation, when run until convergence, resolves the attacks, albeit with a slight degradation for high T values. This is consistent with its physics-based design, showing its robustness to adaptive attacks.

output. These demonstrate that a single-step attack cannot surpass the iterative-based ones in terms of attack success, and similarly, increasing the perturbation bound leads to more severe degradation with PGD. These sanity checks align with the fact that we used the exact gradient through the steps described in Section 4.1, validating that gradient obfuscation did not happen in our implementation.

F.3 VISUALIZATION OF ADAPTIVE ATTACKS AND MITIGATION

Representative examples showing the performance of the mitigation algorithm for different adaptive attacks generated using Eq. (11) with the unrolled version of $g(\cdot)$ for $T \in \{10, 25, 50, 100\}$ are provided in Fig. 14. The first row shows the results of the baseline reconstruction under both non-adaptive and adaptive attacks for various T . Consistent with Tab. 2, as T increases for the adaptive attack, the baseline deterioration becomes less substantial. The second row shows the performance of the mitigation algorithm when it is unrolled for the same number of T as in the adaptive attack generation. In this case, for lower T , the unrolled mitigation has performance degradation, as expected. Finally, the final row shows results of the iterative mitigation algorithm run until convergence. In all cases, the iterative mitigation algorithm successfully recovers a clean image, owing to its physics-based nature, as discussed in Section 4.2. However, we note that though adaptive attacks have milder effect on the baseline with increasing T , they do deteriorate the iterative mitigation albeit slightly as a function of increasing T .

Table 11: Fine-tuning the λ parameter in Eq. (11) across $T \in \{10, 25\}$.

Unrolls	$\lambda = 1$	$\lambda = 2$	$\lambda = 3$	$\lambda = 5$	$\lambda = 10$
$T = 10$	34.51	34.48	34.41	34.34	34.66
$T = 25$	34.41	34.36	34.40	34.16	34.47

Table 12: Checking gradient obfuscation on the Cor-PD dataset over $T \in \{10, 25\}$.

T	PGD		FGSM
	$(\epsilon = 0.01)$	$(\epsilon = 0.02)$	
10	34.34	33.11	35.17
25	34.16	32.77	35.01

1134 **G PROOF OF THEOREM 1**
 1135

1136 The standard proof techniques for unrolled networks (Liang et al., 2023; Pramanik et al., 2023)
 1137 performs an error propagation analysis through the layers of the network in image domain. However,
 1138 this is insufficient in our case, as it does not capture differences between the behavior of the k-space
 1139 in Ω and Ω^C . Thus, here we present a different analysis approach.

1140 We first present some basic notation and assumptions about multi-coil forward operator, $\mathbf{E}_\Omega \in$
 1141 $\mathbb{C}^{M \times N}$ (Pruessmann et al., 1999; Lustig & Pauly, 2010; Uecker et al., 2014):
 1142

$$1143 \mathbf{E}_\Omega = \begin{bmatrix} \mathbf{F}_\Omega \mathbf{S}_1 \\ \mathbf{F}_\Omega \mathbf{S}_2 \\ \vdots \\ \mathbf{F}_\Omega \mathbf{S}_{n_c} \end{bmatrix}, \quad (15)$$

1144 where \mathbf{F}_Ω is a partial Fourier operator¹, $\mathbf{S}_k \triangleq \text{diag}(\mathbf{s}_k)$ are diagonal matrices corresponding to the
 1145 sensitivity map of the k^{th} coil and n_c is the number of coils. Note that, by design, coil sensitivity
 1146 maps satisfy $\sum_k \mathbf{S}_k \mathbf{S}_k^H = \mathbf{I}$ (Uecker et al., 2014; Demirel et al., 2023a). We also define $\mathbf{E}_{\Omega^C} \in$
 1147 $\mathbb{C}^{N \cdot n_c \times M \times N}$ in an analogous manner. Finally, we note that \mathbf{S}_k are smooth/low-frequency due to the
 1148 physics of the MR acquisition (Pruessmann et al., 1999; Uecker et al., 2014), which will be defined
 1149 more concretely below.

1150 **Lemma 1.1.** *Let $\mathbf{S}_k = \text{diag}(\mathbf{s}_k)$ be smooth, defined as containing most of their energy in L low-
 1151 frequency coefficients in the Fourier domain, i.e. $\sum_{l \notin [-L/2, L/2-1]} |(F\mathbf{s}_k)_l|^2 < \zeta$, and assume Ω
 1152 contains the ACS region with frequencies $[-L, L-1]$. Then*

$$1153 \|\mathbf{E}_\Omega \mathbf{E}_{\Omega^C}^H\|_2 < c_1 \sqrt{\zeta} + c_2 \zeta$$

1154 *for constants $c_1 = 2n_c, c_2 = n_c/\sqrt{N}$.*

1155 *Proof.* First note that in the single coil case, where $n_c = 1$ and $\mathbf{S}_1 = \mathbf{I}$, i.e. $\mathbf{E}_\Omega = \mathbf{F}_\Omega$ and
 1156 $\mathbf{E}_{\Omega^C} = \mathbf{F}_{\Omega^C}$, we trivially have $\mathbf{F}_\Omega \mathbf{F}_{\Omega^C}^H = \mathbf{0}$ by the orthonormality of the rows of the discrete
 1157 Fourier matrix. We will build on this intuition using the smoothness of \mathbf{S}_k along the way. To this
 1158 end, note

$$1159 \mathbf{E}_\Omega \mathbf{E}_{\Omega^C}^H = \begin{bmatrix} \mathbf{F}_\Omega \mathbf{S}_1 \\ \mathbf{F}_\Omega \mathbf{S}_2 \\ \vdots \\ \mathbf{F}_\Omega \mathbf{S}_{n_c} \end{bmatrix} \left[\begin{array}{cccc} \mathbf{S}_1^H \mathbf{F}_{\Omega^C}^H & \mathbf{S}_2^H \mathbf{F}_{\Omega^C}^H & \dots & \mathbf{S}_{n_c}^H \mathbf{F}_{\Omega^C}^H \end{array} \right] \quad (16)$$

1160 has a block structure with $(p, q)^{\text{th}}$ block \mathbf{B}_{pq} given by

$$1161 \mathbf{B}_{pq} = \mathbf{F}_\Omega \mathbf{S}_p \mathbf{S}_q^H \mathbf{F}_{\Omega^C}^H.$$

1162 Note by block Frobenius inequality

$$1163 \|\mathbf{E}_\Omega \mathbf{E}_{\Omega^C}^H\|_2^2 \leq \sum_{p,q} \|\mathbf{B}_{pq}\|_2^2 \quad (17)$$

1164 Next, we will consider the norm of the $(p, q)^{\text{th}}$ block:

$$1165 \mathbf{F}_\Omega \mathbf{S}_p \mathbf{S}_q^H \mathbf{F}_{\Omega^C}^H = \mathbf{P}_\Omega \underbrace{(\mathbf{F} \mathbf{S}_p \mathbf{S}_q^H \mathbf{F}^H)}_{\triangleq \mathbf{C}_{pq}} \mathbf{P}_{\Omega^C}^H,$$

1166 where \mathbf{C}_{pq} implements a circulant matrix implementing a circular convolution operation with kernel

$$1167 \mathbf{b}_{pq} = \mathbf{F}(\mathbf{s}_p \odot \bar{\mathbf{s}}_q) = \frac{1}{\sqrt{N}} \underbrace{\mathbf{F} \mathbf{s}_p}_{\mathbf{a}_p} \circledast \underbrace{\mathbf{F} \bar{\mathbf{s}}_q}_{\bar{\mathbf{a}}_q}.$$

1168 ¹We will use $\mathbf{F} \in \mathbb{C}^{N \times N}$ to denote the full discrete Fourier transform matrix. This allows us to equivalently
 1169 define $\mathbf{F}_\Omega \triangleq \mathbf{P}_\Omega \mathbf{F}$, where \mathbf{P}_Ω is a binary mask specifying the sampling pattern Ω .

1188 Here \cdot denotes elementwise complex conjugation, \odot denotes the elementwise Hadamard product
 1189 and \circledast denotes circular convolution. Now note
 1190

$$1191 \|\mathbf{B}_{pq}\|_2 \leq \|\mathbf{C}_{pq}\|_2 = \max_j |(\mathbf{b}_{pq})_j| = \max_j \left| \frac{1}{\sqrt{N}} \sum_l \mathbf{a}_{p,l} \overline{\mathbf{a}_{q,l-j}} \right|$$

1193 To calculate this last term, we decompose \mathbf{a}_p and \mathbf{a}_q into their low-frequency (between
 1194 $[-L/2, L/2 - 1]$) and the remaining high-frequency components, noting $\|\mathbf{a}_k^{\text{high}}\|_2^2 \leq \zeta$. Then
 1195

$$1196 \mathbf{b}_{pq} = \frac{1}{\sqrt{N}} [(\mathbf{a}_p^{\text{low}} \circledast \overline{\mathbf{a}_q^{\text{low}}})_j + (\mathbf{a}_p^{\text{low}} \circledast \overline{\mathbf{a}_q^{\text{high}}})_j + (\mathbf{a}_p^{\text{high}} \circledast \overline{\mathbf{a}_q^{\text{low}}})_j + (\mathbf{a}_p^{\text{high}} \circledast \overline{\mathbf{a}_q^{\text{high}}})_j].$$

1199 Using Cauchy-Schwarz inequality:

$$1200 \left| (\mathbf{a}_p^{\text{low}} \circledast \overline{\mathbf{a}_q^{\text{high}}})_j \right| \leq \|\mathbf{a}_p^{\text{low}}\|_2 \|\mathbf{a}_q^{\text{high}}\|_2 < \sqrt{\zeta N}.$$

1202 Similarly for the two high-frequency terms:

$$1204 \left| (\mathbf{a}_p^{\text{high}} \circledast \overline{\mathbf{a}_q^{\text{high}}})_j \right| \leq \|\mathbf{a}_p^{\text{high}}\|_2 \|\mathbf{a}_q^{\text{high}}\|_2 < \zeta.$$

1205 Finally the convolution of the two low-frequency terms are supported between $[-L, L - 1]$. Since all
 1206 these frequencies are in Ω , then these vanish for the values picked up in \mathbf{B}_{pq} by the corresponding
 1207 masks, leading to

$$1208 \|\mathbf{B}_{pq}\|_2 < 2\sqrt{\zeta} + \zeta/\sqrt{N}.$$

1210 Combining this with Eq. (17) yields

$$1212 \|\mathbf{E}_\Omega \mathbf{E}_{\Omega^C}^H\|_2 < n_c (2\sqrt{\zeta} + \zeta/\sqrt{N}). \quad (18)$$

□

1215 **Corollary 1.1.** *Under the same conditions, we have $\|\mathbf{E}_{\Omega^C}\|_2 < n_c \zeta / \sqrt{N}$.*

1216 This corollary is helpful in establishing

$$1218 \|\mathbf{E}_\Omega \mathbf{x}\|_2^2 = \|\mathbf{x}\|_2^2 - \|\mathbf{E}_{\Omega^C} \mathbf{x}\|_2^2 \implies \|\mathbf{x}\|_2 \leq \frac{\|\mathbf{E}_\Omega \mathbf{x}\|_2}{\sqrt{1 - \|\mathbf{E}_{\Omega^C}\|_2^2}}, \quad (19)$$

1221 for $n_c \zeta < \sqrt{N}$. Note trivially $\|\mathbf{E}_{\Omega^C}\|_2 \leq 1$ by the properties of the discrete Fourier transform and
 1222 since $\sum_k \mathbf{S}_K \mathbf{S}_K^H = \mathbf{I}$. We also note in our experiments $n_c \leq 20$, while $\sqrt{N} \geq 320$.

1223 **Lemma 1.2.** $\mathbf{E}_\Omega (\mathbf{E}_\Omega^H \mathbf{E}_\Omega + \mu \mathbf{I})^{-1} = (\mu \mathbf{I} + \mathbf{E}_\Omega \mathbf{E}_\Omega^H)^{-1} \mathbf{E}_\Omega$

1225 *Proof.* By Woodbury's matrix identity, we have

$$1227 (\mathbf{E}_\Omega^H \mathbf{E}_\Omega + \mu \mathbf{I})^{-1} = \frac{\mathbf{I}}{\mu} - \frac{\mathbf{I}}{\mu} \mathbf{E}_\Omega^H (\mu \mathbf{I} + \mathbf{E}_\Omega \mathbf{E}_\Omega^H)^{-1} \mathbf{E}_\Omega \quad (20)$$

1229 Then

$$1231 \mathbf{E}_\Omega (\mathbf{E}_\Omega^H \mathbf{E}_\Omega + \mu \mathbf{I})^{-1} = \frac{\mathbf{E}_\Omega}{\mu} - \frac{\mathbf{E}_\Omega \mathbf{E}_\Omega^H}{\mu} (\mu \mathbf{I} + \mathbf{E}_\Omega \mathbf{E}_\Omega^H)^{-1} \mathbf{E}_\Omega$$

$$1232 = \left(\frac{\mu \mathbf{I} + \mathbf{E}_\Omega \mathbf{E}_\Omega^H}{\mu} - \frac{\mathbf{E}_\Omega \mathbf{E}_\Omega^H}{\mu} \right) (\mu \mathbf{I} + \mathbf{E}_\Omega \mathbf{E}_\Omega^H)^{-1} \mathbf{E}_\Omega$$

$$1233 = (\mu \mathbf{I} + \mathbf{E}_\Omega \mathbf{E}_\Omega^H)^{-1} \mathbf{E}_\Omega$$

□

1238 **Proof of Theorem 1.** We will next do our error propagation analysis. We will use $\mathbf{x} = \mathbf{E}_\Omega^H \mathbf{E}_\Omega \mathbf{x} + \mathbf{E}_{\Omega^C}^H \mathbf{E}_{\Omega^C} \mathbf{x}$ to decompose the contributions from Ω and Ω^C frequencies. Note the former are always
 1239 brought back close to the measurements due to the presence of DF units, while the latter does not
 1240 follow this behavior. Let $\mathbf{x}^{(k)}$ and $\mathbf{z}^{(k)}$ denote the DF unit output and the proximal operator output
 1241

of the k^{th} unroll of the PD-DL network for the *clean input* \mathbf{y}_Ω . Similarly $\tilde{\mathbf{x}}^{(k)}$ and $\tilde{\mathbf{z}}^{(k)}$ denote the DF unit output and the proximal operator output of the k^{th} unroll of the PD-DL network for the *perturbed input* $\mathbf{y}_\Omega + \mathbf{w}$. Analogously, we will define $\mathbf{y}_\Omega^{(k)} = \mathbf{E}_\Omega \mathbf{x}^{(k)}$ and $\tilde{\mathbf{y}}_\Omega^{(k)} = \mathbf{E}_\Omega \tilde{\mathbf{x}}^{(k)}$. We will also use singular value decompositions for $\mathbf{E}_\Omega = \mathbf{U} \Sigma_\Omega \mathbf{V}^H$ and $\mathbf{E}_{\Omega^C} = \mathbf{U}' \Sigma_{\Omega^C} \mathbf{V}'^H$. Finally, we will denote the largest and smallest singular values of \mathbf{E}_Ω by σ_{\max}^Ω and σ_{\min}^Ω respectively, and those of \mathbf{E}_{Ω^C} by $\sigma_{\max}^{\Omega^C}$ and $\sigma_{\min}^{\Omega^C}$ analogously. With these in place, we have:

$$\begin{aligned}
\|(\tilde{\mathbf{y}}_\Omega^{(k)} - \mathbf{y}_\Omega^{(k)})\|_2 &= \|\mathbf{E}_\Omega(\tilde{\mathbf{x}}^{(k)} - \mathbf{x}^{(k)})\|_2 \\
&= \|\mathbf{E}_\Omega(\mathbf{E}_\Omega^H \mathbf{E}_\Omega + \mu \mathbf{I})^{-1} [(\mathbf{E}_\Omega^H \tilde{\mathbf{y}}_\Omega^{(k)} + \mu \tilde{\mathbf{z}}^{(k)}) - (\mathbf{E}_\Omega^H \mathbf{y}_\Omega^{(k)} + \mu \mathbf{z}^{(k)})]\|_2 \\
&= \|\mathbf{E}_\Omega(\mathbf{E}_\Omega^H \mathbf{E}_\Omega + \mu \mathbf{I})^{-1} [\mathbf{E}_\Omega^H \mathbf{w} + \mu(\tilde{\mathbf{z}}^{(k)} - \mathbf{z}^{(k)})]\|_2 \\
&= \|\mathbf{E}_\Omega(\mathbf{E}_\Omega^H \mathbf{E}_\Omega + \mu \mathbf{I})^{-1} [\mathbf{E}_\Omega^H \mathbf{w} + \mu \mathbf{E}_\Omega^H \mathbf{E}_\Omega(\tilde{\mathbf{z}}^{(k)} - \mathbf{z}^{(k)})] + \\
&\quad \mathbf{E}_\Omega(\mathbf{E}_\Omega^H \mathbf{E}_\Omega + \mu \mathbf{I})^{-1} [\mu \mathbf{E}_{\Omega^C}^H \mathbf{E}_{\Omega^C}(\tilde{\mathbf{z}}^{(k)} - \mathbf{z}^{(k)})]\|_2 \\
&\leq \|\mathbf{E}_\Omega(\mathbf{E}_\Omega^H \mathbf{E}_\Omega + \mu \mathbf{I})^{-1} [\mathbf{E}_\Omega^H \mathbf{w} + \mu \mathbf{E}_\Omega^H \mathbf{E}_\Omega(\tilde{\mathbf{z}}^{(k)} - \mathbf{z}^{(k)})]\|_2 + \\
&\quad \|\mathbf{E}_\Omega(\mathbf{E}_\Omega^H \mathbf{E}_\Omega + \mu \mathbf{I})^{-1} [\mu \mathbf{E}_{\Omega^C}^H \mathbf{E}_{\Omega^C}(\tilde{\mathbf{z}}^{(k)} - \mathbf{z}^{(k)})]\|_2. \quad (21)
\end{aligned}$$

Now we derive a bound for the second term, which characterizes the effect of \mathbf{E}_Ω on the contributions from $\mathbf{E}_{\Omega^C}^H \mathbf{E}_{\Omega^C}$:

$$\begin{aligned}
&\|\mathbf{E}_\Omega(\mathbf{E}_\Omega^H \mathbf{E}_\Omega + \mu \mathbf{I})^{-1} [\mu \mathbf{E}_{\Omega^C}^H \mathbf{E}_{\Omega^C}(\tilde{\mathbf{z}}^{(k)} - \mathbf{z}^{(k)})]\|_2 \\
&\xrightarrow{\text{Lemma 1.2}} = \|(\mu \mathbf{I} + \mathbf{E}_\Omega \mathbf{E}_\Omega^H)^{-1} \mathbf{E}_\Omega [\mu \mathbf{E}_{\Omega^C}^H \mathbf{E}_{\Omega^C}(\tilde{\mathbf{z}}^{(k)} - \mathbf{z}^{(k)})]\|_2 \\
&\leq \mu \|(\mu \mathbf{I} + \mathbf{E}_\Omega \mathbf{E}_\Omega^H)^{-1}\|_2 \|\mathbf{E}_\Omega \mathbf{E}_{\Omega^C}^H\|_2 \|\mathbf{E}_{\Omega^C}(\tilde{\mathbf{z}}^{(k)} - \mathbf{z}^{(k)})\|_2 \\
&\leq \mu \|(\mu \mathbf{I} + \mathbf{U} \Sigma_\Omega \mathbf{V}^H \mathbf{V} \Sigma_\Omega \mathbf{U}^H)^{-1}\|_2 \|\mathbf{E}_\Omega \mathbf{E}_{\Omega^C}^H\|_2 \|\mathbf{E}_{\Omega^C}\|_2 m \|\tilde{\mathbf{x}}^{(k-1)} - \mathbf{x}^{(k-1)}\|_2 \\
&\leq \mu \|\mathbf{U}(\Sigma_\Omega^2 + \mu \mathbf{I})^{-1} \mathbf{U}^H\|_2 \|\mathbf{E}_\Omega \mathbf{E}_{\Omega^C}^H\|_2 \|\mathbf{E}_{\Omega^C}\|_2 m \|\tilde{\mathbf{x}}^{(k-1)} - \mathbf{x}^{(k-1)}\|_2 \\
&\xrightarrow{\text{Corollary 1.1}} \leq \mu \|\Sigma_\Omega^2 + \mu \mathbf{I}\|_2 \|\mathbf{E}_\Omega \mathbf{E}_{\Omega^C}^H\|_2 \frac{m \|\mathbf{E}_{\Omega^C}\|_2}{\sqrt{1 - \|\mathbf{E}_{\Omega^C}\|_2^2}} \|\tilde{\mathbf{y}}_\Omega^{(k-1)} - \mathbf{y}_\Omega^{(k-1)}\|_2 \\
&\leq \frac{\mu}{\mu + (\sigma_{\min}^\Omega)^2} \|\mathbf{E}_\Omega \mathbf{E}_{\Omega^C}^H\|_2 \frac{m \sigma_{\max}^{\Omega^C}}{\sqrt{1 - \sigma_{\max}^{\Omega^C}}} \|\tilde{\mathbf{y}}_\Omega^{(k-1)} - \mathbf{y}_\Omega^{(k-1)}\|_2 \\
&\xrightarrow{\text{Lemma 1.1}} \leq \underbrace{\frac{\mu}{\mu + (\sigma_{\min}^\Omega)^2} \left(2n_c \sqrt{\zeta} + \frac{\zeta}{\sqrt{N}} \right)}_{\alpha_\Omega} \frac{m \sigma_{\max}^{\Omega^C}}{\sqrt{1 - \sigma_{\max}^{\Omega^C}}} \|\tilde{\mathbf{y}}_\Omega^{(k-1)} - \mathbf{y}_\Omega^{(k-1)}\|_2 \quad (22)
\end{aligned}$$

Next we consider the first term of Eq. (21), which characterizes the effect of \mathbf{E}_Ω on the contributions from $\mathbf{E}_\Omega^H \mathbf{E}_\Omega$:

$$\begin{aligned}
&\|\mathbf{E}_\Omega(\mathbf{E}_\Omega^H \mathbf{E}_\Omega + \mu \mathbf{I})^{-1} [\mathbf{E}_\Omega^H \mathbf{w} + \mu \mathbf{E}_\Omega^H \mathbf{E}_\Omega(\tilde{\mathbf{z}}^{(k)} - \mathbf{z}^{(k)})]\|_2 \\
&\leq \|\mathbf{E}_\Omega(\mathbf{E}_\Omega^H \mathbf{E}_\Omega + \mu \mathbf{I})^{-1} \mathbf{E}_\Omega^H \mathbf{w}\|_2 + \mu \|\mathbf{E}_\Omega(\mathbf{E}_\Omega^H \mathbf{E}_\Omega + \mu \mathbf{I})^{-1} \mathbf{E}_\Omega^H \mathbf{E}_\Omega(\tilde{\mathbf{z}}^{(k)} - \mathbf{z}^{(k)})\|_2 \\
&\leq \|\mathbf{E}_\Omega(\mathbf{E}_\Omega^H \mathbf{E}_\Omega + \mu \mathbf{I})^{-1} \mathbf{E}_\Omega^H \mathbf{w}\|_2 + \mu \|\mathbf{E}_\Omega(\mathbf{E}_\Omega^H \mathbf{E}_\Omega + \mu \mathbf{I})^{-1} \mathbf{E}_\Omega^H \mathbf{E}_\Omega\|_2 \|\tilde{\mathbf{z}}^{(k)} - \mathbf{z}^{(k)}\|_2 \\
&\leq \|\mathbf{E}_\Omega(\mathbf{E}_\Omega^H \mathbf{E}_\Omega + \mu \mathbf{I})^{-1} \mathbf{E}_\Omega^H \mathbf{w}\|_2 + \mu \|\mathbf{E}_\Omega(\mathbf{E}_\Omega^H \mathbf{E}_\Omega + \mu \mathbf{I})^{-1} \mathbf{E}_\Omega^H \mathbf{E}_\Omega\|_2 m \|\tilde{\mathbf{x}}^{(k-1)} - \mathbf{x}^{(k-1)}\|_2
\end{aligned}$$

$$\begin{aligned}
&\leq \left\| \mathbf{U} \Sigma_{\Omega} \mathbf{V}^H \left(\mathbf{V} \Sigma_{\Omega} \mathbf{U}^H \mathbf{U} \Sigma_{\Omega} \mathbf{V}^H + \mu \mathbf{I} \right)^{-1} \mathbf{V} \Sigma_{\Omega} \mathbf{U}^H \mathbf{w} \right\|_2 \\
&+ \left\| \mathbf{U} \Sigma_{\Omega} \mathbf{V}^H \left(\mathbf{V} \Sigma_{\Omega} \mathbf{U}^H \mathbf{U} \Sigma_{\Omega} \mathbf{V}^H + \mu \mathbf{I} \right)^{-1} \mathbf{V} \Sigma_{\Omega} \mathbf{U}^H \mathbf{U} \Sigma_{\Omega} \mathbf{V}^H \right\|_2 m \left\| (\tilde{\mathbf{x}}^{(k-1)} - \mathbf{x}^{(k-1)}) \right\|_2 \\
&\leq \|\Sigma_{\Omega}\|_2^2 \|(\Sigma_{\Omega}^2 + \mu \mathbf{I})^{-1}\|_2 \|\mathbf{w}\|_2 + \frac{m \|\Sigma_{\Omega}\|_2^3 \|(\Sigma_{\Omega}^2 + \mu \mathbf{I})^{-1}\|_2}{\sqrt{1 - \|\mathbf{E}_{\Omega^C}\|_2^2}} \left\| \tilde{\mathbf{y}}_{\Omega}^{(k-1)} - \mathbf{y}_{\Omega}^{(k-1)} \right\|_2 \\
&\leq \underbrace{\frac{(\sigma_{\max}^{\Omega})^2}{(\sigma_{\min}^{\Omega})^2 + \mu}}_{\beta} \|\mathbf{w}\|_2 + \underbrace{\frac{m(\sigma_{\max}^{\Omega})^3}{(\sigma_{\min}^{\Omega})^2 + \mu} \cdot \sqrt{\frac{1}{1 - (\sigma_{\max}^{\Omega})^2}}}_{\alpha_{\Omega}} \left\| \tilde{\mathbf{y}}_{\Omega}^{(k-1)} - \mathbf{y}_{\Omega}^{(k-1)} \right\|_2 \quad (23)
\end{aligned}$$

Combining these with Eq. (21), the recursive relation across unrolls is given by:

$$\left\| \tilde{\mathbf{y}}_{\Omega}^{(k)} - \mathbf{y}_{\Omega}^{(k)} \right\|_2 \leq \beta \|\mathbf{w}\|_2 + (\alpha_{\Omega} + \alpha_{\Omega^C}) \left\| \tilde{\mathbf{y}}_{\Omega}^{(k-1)} - \mathbf{y}_{\Omega}^{(k-1)} \right\|_2 \quad (24)$$

Evaluating the recursion through the K unrolls yields:

$$\|\mathbf{E}_{\Omega}(\tilde{\mathbf{x}} - \mathbf{x})\|_2 = \left\| \tilde{\mathbf{y}}_{\Omega}^{(K)} - \mathbf{y}_{\Omega}^{(K)} \right\|_2 \leq \left(\beta \frac{1 - (\alpha_{\Omega} + \alpha_{\Omega^C})^K}{1 - (\alpha_{\Omega} + \alpha_{\Omega^C})} + (\alpha_{\Omega} + \alpha_{\Omega^C})^K \right) \|\mathbf{w}\|_2 \quad (25)$$

H ABLATION STUDY

As discussed in Section 4.3, we analyzed the number of reconstruction stages for mitigation. By extending the number of reconstruction stages, we can reformulate this by updating the second term in the loss function in Eq. (10) to include more reconstruction stages, for instance with 3 cyclic stages instead of 2 given in Eq. (10):

$$\begin{aligned}
&\arg \min_{\mathbf{r}' : \|\mathbf{r}'\|_p \leq \epsilon} \mathbb{E}_{\Gamma} \mathbb{E}_{\Delta} \left[\left\| (\mathbf{E}_{\Omega}^H)^{\dagger} (\mathbf{z}_{\Omega} + \mathbf{r}') - \right. \right. \\
&\left. \left. \mathbf{E}_{\Omega} f \left(\mathbf{E}_{\Gamma}^H \left(\mathbf{E}_{\Gamma} f \left(\mathbf{E}_{\Delta}^H \left(\mathbf{E}_{\Delta} f(\mathbf{z}_{\Omega} + \mathbf{r}', \mathbf{E}_{\Omega}; \theta) + \tilde{\mathbf{n}} \right), \mathbf{E}_{\Delta}; \theta \right) + \tilde{\mathbf{n}}, \mathbf{E}_{\Gamma} \right); \theta \right) \right\|_2 \right]. \quad (26)
\end{aligned}$$

Empirically, in our implementation, we carry out the expectation over all possible permutations without repeating any patterns. As a result, the error propagated to the last stage becomes larger, as we rely more on synthesized data. In turn, this makes the optimization process harder, deteriorating the results, as shown in Fig. 15. Consequently, in addition to these performance issues, the computation costs of adding more cyclic reconstruction is often impractical, leading to the conclusion that 2-cyclic stages as in Eq. (10) are sufficient.



Figure 15: Ablation study on the number of stages for cyclic measurement consistency. Two reconstruction levels (left) outperform deeper variants (middle, right), as additional stages overly rely on synthesized k-space data.

1350 1351 1352 1353 1354 1355 I COMPARISONS TO OTHER TRAINING-FREE DEFENSE METHODOLOGIES

1356 This section explores other training-free mitigation approaches against adversarial attacks and their
 1357 implementation details. We compare our method to JPEG compression, total-variation (TV) mini-
 1358 mization, randomized smoothing (RS) (Cohen et al., 2019) on the input.

1359 **JPEG Compression.** This is an input transform method that is popular for defending against
 1360 adversarial attacks (Aydemir et al., 2018; Cucu et al., 2023). JPEG uses discrete cosine transform
 1361 (DCT) for image compression, which inherently modifies the perturbed input without substantially
 1362 changing its visual characteristics, potentially away from its worst-case behavior. We adopt the
 1363 standard JPEG compression pipeline for complex-valued MRI images by applying the transform
 1364 separately to the positive and negative parts of both the real and imaginary components of $\mathbf{z}_\Omega^P =$
 1365 $\mathbf{z}_\Omega + \mathbf{r}$. The four compressed channels are recombined to reconstruct the complex-valued data.

1366 **TV Minimization/Denoising** This is another input-space transformation that has been employed
 1367 against adversarial perturbations (Sheikh & Zafar, 2024). In particular, it optimizes the following
 1368 denoising objective:

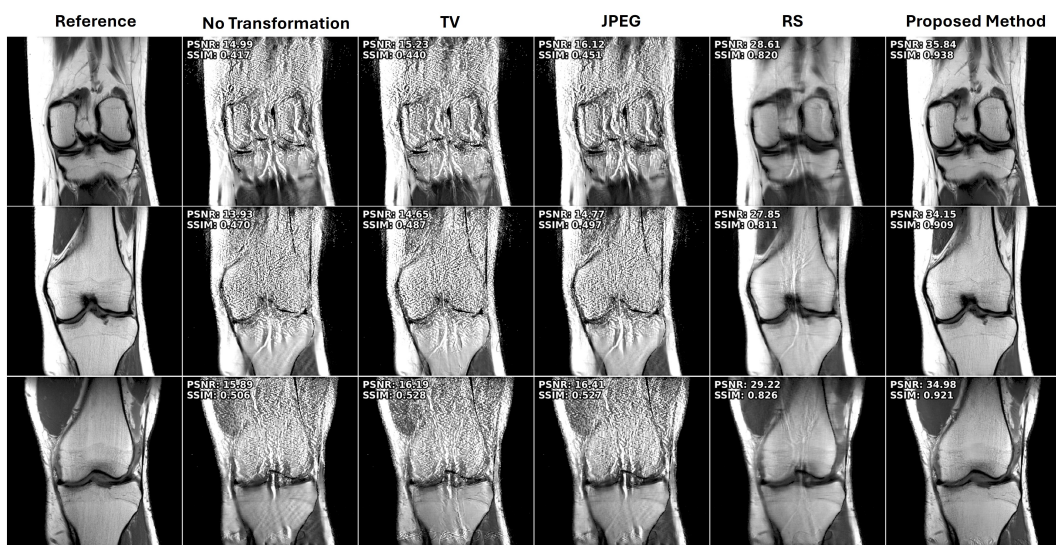
$$1369 \min_{\mathbf{z}} \|\mathbf{z}_\Omega^P - \mathbf{z}\|_2^2 + \beta TV(\mathbf{z}) \quad (27)$$

1370 where the $TV(\cdot)$ is the total-variation norm formulated as follow:

$$1371 TV(\mathbf{x}) = \sum_{i,j} (|\mathbf{x}_{i+1,j} - \mathbf{x}_{i,j}| + |\mathbf{x}_{i,j+1} - \mathbf{x}_{i,j}|). \quad (28)$$

1372 We followed this formulation to denoise the adversarially perturbed input. In particular, given the
 1373 perturbed input \mathbf{z}_Ω^P we solve Eq. (27) using $\lambda = 0.01$ and 5 iterations.

1374 Note that the application of TV denoising as a defense mechanism for MRI reconstruction is not
 1375 straightforward, as the input image \mathbf{z}_Ω is inherently aliased due to undersampling. In contrast, TV
 1376 regularization guides its output to a piecewise smooth output to minimize the objective in Eq. (27).
 1377 Thus if run with a large λ or for a large number of iterations, the aliasing artifacts will be changed,
 1378 breaking the relationship with the forward operator \mathbf{E}_Ω in Eq. (1). Note a similar concern ap-
 1379 plies to other image-domain denoising-based input purification strategies, such as diffusion puri-
 1380 fication (Alkhouri et al., 2023; 2024) discussed further below, as the diffusion purification will push
 1381 the output to the clean data manifold, losing the aliasing information that defines the relationship
 1382 in Eq. (1). In summary, for TV minimization, the iteration count was intentionally kept small, as
 1383 further optimization begins to de-alias the zero-filled image, further degrading the overall quality of
 1384 the subsequent PD-DL reconstruction.



1402 1403 Figure 16: Representative results of different training-free methodologies applied on the perturbed
 1404 inputs. Reconstructions show the proposed method outperforms existing classical approaches.

1404
1405
1406
1407
1408
1409
1410
1411
1412
1413
1414
1415
1416
1417
1418
1419
1420
1421
1422
1423
1424
1425
1426
1427
1428
1429
1430
1431
1432
1433
1434
1435
1436
1437
1438
1439
1440
1441
1442
1443
1444
1445
1446
1447
1448
1449
1450
1451
1452
1453
1454
1455
1456
1457
Table 13: λ fine-tuning

Metric	MoDL	$\lambda = 0.01$	$\lambda = 0.02$	$\lambda = 0.05$	$\lambda = 0.1$	$\lambda = 0.2$	$\lambda = 0.3$
PSNR	16.30	22.92	23.05	24.09	27.38	30.71	29.65
SSIM	0.486	0.622	0.628	0.670	0.777	0.858	0.851

Randomized Smoothing (RS) RS was first introduced for classification tasks (Cohen et al., 2019) and was later extended to regression settings (Rekavandi et al., 2024). In MRI reconstruction, given a pre-trained network $f(\cdot, \cdot; \theta)$, RS is performed as (Liang et al., 2023):

$$f_{\text{smooth}}(\mathbf{z}_{\Omega}^p, \mathbf{E}_{\Omega}; \theta) = \mathbb{E}_{\xi \sim \mathcal{N}(\mathbf{0}, \lambda \mathbf{I})} \left[f(\mathbf{E}_{\Omega}^H(\mathbf{y}_{\Omega}^p + \xi), \mathbf{E}_{\Omega}; \theta) \right] \quad (29)$$

where λ is a tuning parameter that control the trade-off between accuracy and robustness. In our implementation, we generated 50 zero-mean Gaussian noise samples, added them to the perturbed k-space representation \mathbf{y}_{Ω}^p , and reconstructed each using the pre-trained MoDL. The final output was obtained by averaging these reconstructions. For noise injection, λ was adjusted to fine-tune performance across the dataset. Tab. 13 shows the population metrics on different λ values. Representative reconstruction results and the population metrics of each method on the test set are shown in Fig. 16 and Tab. 14, respectively. Both JPEG and TV denoising methods fail to mitigate the attack in a meaningful manner. RS outperforms these two input transformation methods, but still substantially falls short of the proposed method both quantitatively and visually with extensive blurring due to the high-level noise and inherent averaging.

J COMPARISON TO DIFFUSION PURIFICATION FOR MRI RECONSTRUCTION

Diffusion purification (Nie et al., 2022) is a technique proposed to mitigate the effect of adversarial samples before they are used in downstream tasks. In particular, it works by adding scheduled noise to an adversarial example up to a diffusion step t_1 , causing the clean and adversarial distributions to progressively converge (e.g. at $t_1 = T$, both distributions become standard Gaussian). Then the method performs t_1 reverse diffusion steps to purify the corrupted adversarial sample. In this way, purification enhances robustness in tasks such as classification (Nie et al., 2022). However, the application of diffusion purification for MRI reconstruction is not straightforward. As mentioned in the TV denoising subsection, diffusion models are trained to learn the distribution of clean fully-sampled data. Thus, if one noises the undersampled zerofilled images (aliased data) and tries to run the reverse diffusion process on this, it will inevitably push the output towards the clean data manifold, which will in turn no longer be consistent with the forward model (and the inverse problem objective). An early work (Alkhouri et al., 2024) considered diffusion purification for the MRI reconstruction problem studied here, and showed that even after purification, a fine-tuning step is required on MoDL network to handle the mismatch between the aliased images and score model trained on clean images. A more comprehensive version of this work (Alkhouri et al., 2023) by the same authors further replaced the noising-denoising purification with a full diffusion model-based ScoreMRI reconstruction (Chung & Ye, 2022), combined with yet another fine-tuned MoDL network. Note in both setups: 1) There is an inherent mismatch between attack generation (on baseline MoDL network) and reconstruction (with two separate reconstructions including ScoreMRI and fine-tuned MoDL), 2) The method is not training-free, as it requires fine-tuning of the MoDL network, 3) The method was never verified against adaptive attacks, which is the gold standard attack technique considered extensively in our work.

Table 14: Comparison of different input-transformation defenses on the Cor-PD dataset, in presence of perturbation. Mean of the population metrics are reported.

Dataset	Metric	MoDL	Input TV + MoDL	Input JPEG + MoDL	Input RS + MoDL	Proposed Method + MoDL
Cor-PD	PSNR	16.30	16.36	17.29	30.71	35.14
	SSIM	0.486	0.488	0.509	0.858	0.921

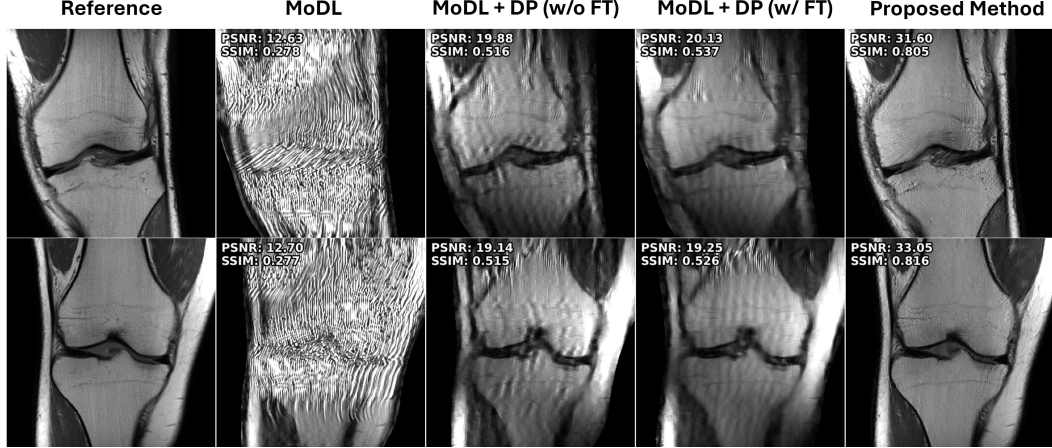


Figure 17: Comparison of proposed method with diffusion purification (Alkhouri et al., 2023). While fine-tuning improves the reconstruction quality of the diffusion purification approach, it still does not surpass the performance of our proposed method.

Nonetheless, even though these approaches (Alkhouri et al., 2023; 2024) are not training-free, to provide a more complete comparison, we additionally implemented diffusion-based adversarial purification pipelines in (Alkhouri et al., 2023), which as discussed earlier is the more comprehensive preprint extending on (Alkhouri et al., 2024). In particular, we reproduced the diffusion purification pipeline, using our own training sets and unrolled reconstruction models, while following the purification description in (Alkhouri et al., 2023). To do so, we first re-trained MoDL, as our baseline $f(\cdot, \cdot; \theta)$, on Cor-PD knee data at a matrix size of 320×320 (instead of 332×320 used in the main text) to ensure compatibility with the matrix sizes expected by the pretrained diffusion model. An acceleration rate of 4 with a random sampling mask, with 24 ACS center lines was used. Second, we generated noisy samples by adding Gaussian noise to the clean zero-filled images, and then passed them through diffusion purification $DP_\phi(\cdot, \cdot, \cdot)$ step described in Alg.2 (Alkhouri et al., 2023) to obtain the purified outputs. Here ϕ specifies the diffusion model (DM) parameters. In particular:

$$\mathbf{z}_\Omega^{\text{pur}} = DP_\phi(\mathbf{z}_\Omega + \mathbf{w}, \mathbf{E}_\Omega, N_r)$$

where $\mathbf{w} \sim \mathcal{N}(\mathbf{0}, \sigma^2 \mathbf{I})$ with $\sigma = 0.001$, and $N_r = 150$ is the tuned parameter for corruption/purification. These purified samples are then used to fine-tune the MoDL for the second stage. In other words, the following loss is used to fine-tune the MoDL, initialized from θ :

$$\arg \min_{\theta_{\text{FT}}} \mathbb{E} \left[\mathcal{L}(f(\mathbf{z}_\Omega^{\text{pur}}, \mathbf{E}_\Omega; \theta_{\text{FT}}), \mathbf{x}_{\text{ref}}) \right], \quad (30)$$

Finally, we generated ℓ_∞ perturbation in image domain on \mathbf{z}_Ω with 10 iterations of PGD (Mkadry et al., 2018), using $\epsilon = 0.01$. Following (Alkhouri et al., 2024), the final pipeline for reconstructing the perturbed input (i.e. $\mathbf{z}_\Omega^{\text{pert}}$) is as follows:

$$\mathbf{z}_\Omega^{\text{pur}} = (\mathbf{E}_\Omega^\text{H} \mathbf{E}_\Omega) DP_\phi(\mathbf{z}_\Omega^{\text{pert}}, \mathbf{E}_\Omega, N_r) \quad (31)$$

$$\hat{\mathbf{x}} = f(\mathbf{z}_\Omega^{\text{pur}}, \mathbf{E}_\Omega; \theta_{\text{FT}}) \quad (32)$$

where $\hat{\mathbf{x}}$ is the final reconstruction. Fig. 17 shows the representative reconstructions. Tab. 15 summarizes the population metric on the test set. Note that the population metrics differ from those reported in the main text for Cor-PD, as this experiment uses a different undersampling pattern and a dataset with a matrix size of 320×320 . Furthermore, when comparing MoDL+DP to MoDL itself, we observe an improvement of approximately 34% in PSNR, and 42% in SSIM, which is consistent with the findings reported in (Alkhouri et al., 2023) (where a 34% in PSNR and 19% in SSIM gain

1512 was reported for the knee dataset in their Table 1). Comparing our baseline population metrics with
 1513 those reported in their table (Alkhouri et al., 2023), we observe that our attack setup (strength and
 1514 type) is stronger, leading to greater degradation of the baseline MoDL. Thus, the diffusion purifi-
 1515 cation method results are quantitatively consistent with those reported in (Alkhouri et al., 2023),
 1516 further highlighting the superior performance of our proposed approach.
 1517

1518 K ERROR EVALUATION ON $\{\Omega, \Omega^C\}$ SETS

1519 As discussed in detail in Section 3.1, we expect the reconstruction to remain consistent
 1520 with measurements on Ω locations, both in presence of an attack (as attack is designed to
 1521 be small imperceptible perturbations on these lines) and in the absence of attack (a natu-
 1522 ral property of the PD-DL methods). Thus, the adversarial attack primarily corrupts the
 1523 non-acquired lines (e.g. Ω^C). We first demonstrated this intuition experimentally (Fig. 1a
 1524 and Section 3.1), and also provided rigorous characterization with Theorem 1. We fur-
 1525 ther corroborate these findings with an additional set of results depicted in Fig. 18.
 1526 In particular, for each knee sample from the test set, we
 1527 generate the corresponding worst-case ℓ_∞ perturbation,
 1528 and compute the final reconstructions, \mathbf{x} and $\hat{\mathbf{x}}$, of both
 1529 the clean and perturbed inputs, respectively. We then
 1530 map these onto the k-space locations specified by Ω and
 1531 Ω^C . Finally, we evaluate the ℓ_2 error (normalized to clean
 1532 data) on each of these index sets:
 1533

$$\frac{\|\mathbf{E}_\Omega(\mathbf{x} - \hat{\mathbf{x}})\|_2}{\|\mathbf{E}_\Omega \mathbf{x}\|_2}, \quad \frac{\|\mathbf{E}_{\Omega^C}(\mathbf{x} - \hat{\mathbf{x}})\|_2}{\|\mathbf{E}_\Omega \mathbf{x}\|_2}, \quad (33)$$

1534 As Fig. 18 shows the reconstruction error on the Ω^C lines
 1535 becomes extremely large with a small adversarial pertur-
 1536 bation, while the error on Ω lines is comparatively negli-
 1537 gible, owing to the data fidelity operations in the PD-DL
 1538 network. As aforementioned, Theorem 1 serves the pur-
 1539 pose of formally establishing these intuitions in a rigor-
 1540 ous manner. Thus, it is complementary to the experimental
 1541 insights that we provide here and in
 1542 Section 3.1.
 1543

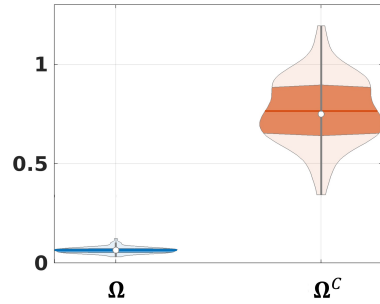
1544 L ADDITIONAL INVERSE PROBLEMS

1545 It is worth investigating whether the
 1546 proposed technique is useful in other
 1547 modalities or inverse problems where
 1548 PD-DL methods are used. First,
 1549 we note that for non-physics-driven
 1550 DL methods, since there is no data-
 1551 consistency term, the expression $\mathbf{E}_\Omega \hat{\mathbf{x}}$ at different stages is not guaranteed to remain close to \mathbf{y}_Ω
 1552 (e.g. measurements). As a result, cyclic consistency does not naturally extend to this setup. How-
 1553 ever, in cases where a data-fidelity term is used in the PD-DL network, then cyclic mitigation strategy
 1554 can be utilized. In particular,

1555 we further examine how the mitigation strategy extends to other inverse problem tasks, such as
 1556 image inpainting. To this end, we used the same VSQP formulation as MoDL in the main text for
 1557 image inpainting. The only modification was using a 3-channel input/output ResNet (as the dataset
 1558 is natural images). The forward operator was a masking operator \mathbf{B}_Ω . We randomly sampled 30%
 1559 of the image as measurements, and trained the network on 1000 images from CelebA (Karras et al.,
 1560 2017) dataset for 100 epochs with normalized ℓ_2 loss. For the synthesized masks at inference, we
 1561 used the remaining 70% of the pixels to generate two additional random Δ_i , ensuring that none of the
 1562 masks share any common pixel locations. We used 10 iterations of PGD for attack generation, with
 1563 $\epsilon = 0.01 \cdot \|\mathbf{E}_\Omega^H \mathbf{y}_\Omega\|_\infty$, and $\alpha = \epsilon/5$, with projection into the ϵ -ball applied after each PGD iteration.
 1564 The representative reconstructions and population metrics over 200 test samples are represented in
 1565 Fig. 19 and Tab. 16, respectively. These show that the proposed method effectively mitigates the

1546 Table 16: Population metrics on the inpainting problem under the ℓ_∞ attack.

Dataset	Metric	MoDL	Proposed + MoDL
CelebA	PSNR	24.05 ± 1.07	30.69 ± 2.25
	SSIM	0.572 ± 0.044	0.873 ± 0.034



1547 Figure 18: Normalized reconstruction
 1548 errors on the Ω and Ω^C sets. The error
 1549 on Ω^C is substantially larger, providing
 1550 quantitative support for Theorem 1.

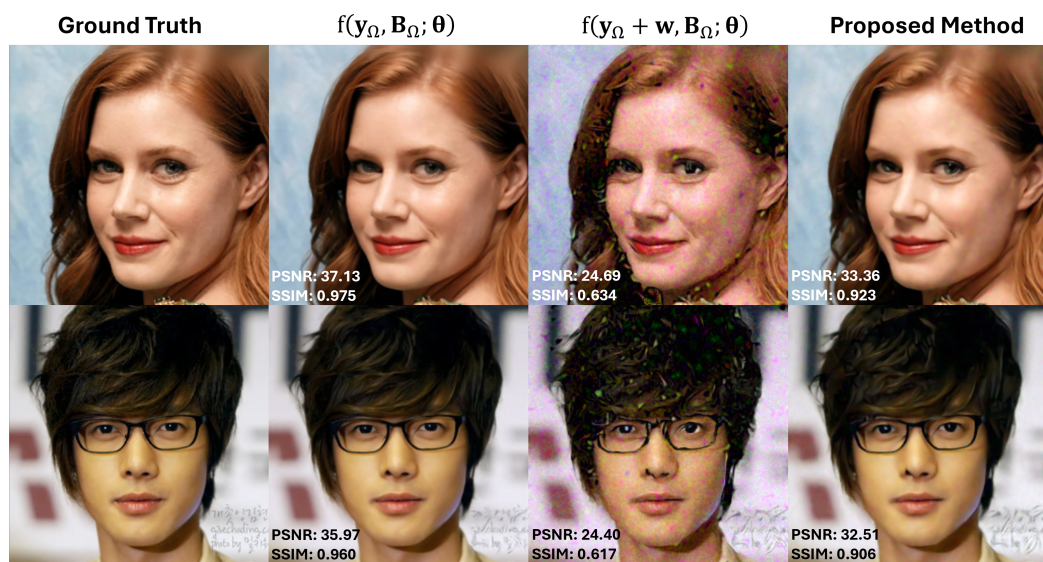


Figure 19: Representative results of random inpainting with 30% sampling.

1566
1567
1568
1569
1570
1571
1572
1573
1574
1575
1576
1577
1578
1579
1580
1581
1582
1583
1584
1585
1586
1587
1588
1589
1590
1591
1592
1593
1594
1595
1596
1597
1598
1599
1600
1601
1602
1603
1604
1605
1606
1607
1608
1609
1610
1611
1612
1613
1614
1615
1616
1617
1618
1619
perturbation and recovers the underlying image structure for the inpainting task on natural images, highlighting its versatility for PD-DL networks across applications.

M RUNTIME COMPARISON

In this section, we further analyze the runtime and computational costs of our method compared with other training-based defense approaches. Tab. 17 summarizes this comparison. The proposed method has a longer inference time because it requires multiple optimization iterations, each involving two forward passes through the network. However, when considering the combined training and inference time, our approach is substantially more efficient than the other two methods. This is because training-based defenses must retrain the network from scratch, and retune hyperparameters, if the attack configuration changes, whereas our method only requires tuning a few optimization parameters, which is far less expensive than full network retraining. Moreover, while we focused on 2D slices in the main text, our mitigation approach is not limited to 2D reconstructions. In particular, we evaluated the computational and memory costs of extending our method to dynamic MRI.

Specifically, we performed dynamic cardiac MRI reconstruction using the OCMR dataset (Chen et al., 2020) and compared the per-iteration runtime and memory usage for 2D and dynamic settings. For the 2D case, we trained a standard MoDL model in a supervised manner using each cardiac phase as an independent sample, with input size $[1, N_x, N_y]$. For the dynamic case, we selected 10 consecutive time frames from each slice and concatenated them along the channel dimension, resulting in an input size of $[10, N_x, N_y]$. Both models were then used within our proposed mitigation framework under adversarial attack. The comparison in Table 18 shows that dynamic reconstruction does not im-

Table 17: Runtime comparison among AT, SMUG, and the proposed method.

Method	Inference Time (sec)	Inference + Training Time (hours)
AT	2.4	~ 20
SMUG	3.1	~ 25.8
Proposed	407	~ 0.1 (407 sec)

Table 18: Memory/time comparison of the proposed method.

Strategy	Memory	Time per Iteration
2D	30.5 GB	2.5 sec
Dynamic	66.5 GB	9.9 sec

1620 pose a substantial additional memory burden. While computation time naturally increases due to
 1621 the higher input dimensionality, the overall scaling remains manageable and lower than the initial
 1622 increase of the input size, indicating that our cyclic consistency-based defense extends naturally to
 1623 higher-dimensional acquisitions.

1624

1625

1626

1627 N ROBUSTNESS UNDER NON-OPTIMAL RECONSTRUCTION CONDITIONS

1628

1629 In this section, we study how the proposed method performs under non-optimal conditions. Such
 1630 conditions may arise in two ways: 1) When the baseline MoDL reconstruction is sub-optimal, and
 1631 2) When the perturbation is generated using a different forward model. For the former case, we note
 1632 that the proposed method naturally inherits pre-trained model’s limitations.

1633 In other words, the mitigation
 1634 strategy can, at best,
 1635 recover the performance
 1636 that the underlying model
 1637 achieves on *clean inputs*,
 1638 since we explore the vicinity
 1639 of the adversary to find
 1640 the non-perturbed version
 1641 of it. This point was discussed in the manuscript when analyzing defense training methods, such as
 1642 AT and SMUG (Section 4.2). For example, SMUG performs poorly under attack and fails to remove
 1643 the resulting artifacts. After applying our mitigation approach, the artifacts are eliminated, but the
 1644 reconstruction remains blurred (Fig. 2).

1645 This limitation is rooted in the pre-trained SMUG model
 1646 itself, because of smoothing with Gaussian noise. To pro-
 1647 vide further evidence supporting this concern, we applied
 1648 the proposed method to very early-stage MoDL weights,
 1649 which are not yet capable of fully recovering fine de-
 1650 tails. Tab. 19 reports the mean PSNR/SSIM of proposed
 1651 mitigation algorithm with different pre-trained MoDLs.
 1652 These results confirm that proposed mitigation approach
 1653 improves the suboptimal reconstruction, without worsen-
 1654 ing the inherent sub-optimality of the baseline.

1655 The later case of non-optimality, however, is more complicated. One probable scenario, can be
 1656 using a different sensitivity coil maps, to generate the perturbation. Under this mismatched coils (or
 1657 forward operator), the generated attack will not be optimum. Since a mismatched coil configuration
 1658 would not produce a good reconstruction for a given sample, the resulting attack would also no
 1659 longer correspond to the true worst-case perturbation (though still within the ϵ -ball), leading to a
 1660 slightly milder adversarial effect. We tested this on a subset of Cor-PD dataset, with results shown
 1661 in Tab. 20. In particular, we generated attacks using coil sensitivity maps from a different subject and
 1662 then applied mitigation using the correct coil maps. Population metrics show that attacks generated
 1663 with mismatched coil maps are slightly milder than those produced with the true coil configuration.

1664

1665

1666

1667

1668

1669

1670

1671

1672

1673

Table 19: Performance under ℓ_∞ attack with different pre-trained MoDL models. The suboptimal MoDL uses the weights from the 1st epoch of training. Mean population metrics are reported.

Dataset	Metric	Suboptimal MoDL	Proposed + Suboptimal MoDL	Proposed + MoDL
Cor-PD	PSNR	18.04	30.19	35.14
	SSIM	0.529	0.856	0.921

Table 20: Comparison of mitigation performance when the attack is generated using different coil sensitivity maps.

Metric	Different Coil	Same Coil
PSNR	34.52	34.51
SSIM	0.911	0.907